FINITE DIFFERENCE SIMULATION OF THE STOKES-BRINKMAN EQUATION FOR TRANSIENT FLOW IN NATURALLY FRACTURED CARBONATE KARST RESERVOIRS

A Dissertation

by

JIE HE

Submitted to the Office of Graduate and Professional Studies of
Texas A&M University
in partial fulfillment of the requirements for the degree of

DOCTOR OF PHILOSOPHY

Chair of Committee,	John E. Killough
Committee Members,	Maria A. Barrufet
	Eduardo Gildin
	Hadi Nasrabadi
Head of Department,	A. Daniel Hill

August 2017

Major Subject: Petroleum Engineering

ABSTRACT

Carbonate reservoirs, despite their simple chemical composition, are notorious for being highly heterogeneous at all scales. The susceptibility of carbonate minerals to chemical changes, mostly dissolution, creates macroscopic pore features like small vugs and big caves which are also collectively known as karst, and mechanical deformation of the brittle carbonate rocks generates natural fractures which may or may not connect those vugs and caves. Carbonate reservoirs may bear karst and fractures having a size range from millimeters to hundreds of meters. Such reservoirs are called naturally fractured carbonate karst reservoirs and commonly found all over the world. Free flow exists in the karst and fractures at multiple levels and couples with Darcy flow in the porous carbonate rocks, making the mathematical modeling and numerical simulation of flow performance in these reservoirs a very challenging problem.

The Stokes-Brinkman equation has been pursued in recent years as a physical yet unified approach toward the simulation of coupled flow in naturally fractured carbonate karst reservoirs, but its application has been somehow restricted to steady-state flow. For the first time, we have proposed a transient Stokes-Brinkman model and lain the theoretical foundation for it, by discovering the applicability of the Stokes-Brinkman equation to transient flow through a detailed examination of its derivation process, and by incorporating a transient material balance equation which proves to be exact in the entire fractured karst reservoir. The finite difference formulation of the transient Stokes-Brinkman model has been derived, again for the first time, and an inhouse reservoir simulator is developed to actually solve this numerical problem.

DEDICATION

To my wife Jian Shen

ACKNOWLEDGMENTS

I am deeply indebted to my advisor, Professor John E. Killough, for his continuous and unreserved help, guidance, and support in the past few years. Without him, I wouldn't have been able to complete this doctoral degree.

I would like to thank Professor Maria A. Barrufet, Professor Eduardo Gildin, and Professor Hadi Nasrabadi for taking their time to sit on my advisory committee, and for their valuable comments and suggestions on my research work.

Special thanks to Dr. Mohamed M. Fadlelmula F., Sunhua Gao, Professor Michael L. Fraim and Dr. Hongqing Song for their collaborations on this project, and to Yang Cao, Dr. Bicheng Yan, Masoud Alfi and other Killough group members for their help during my graduate studies.

I would also like to express my gratitude to the following professors for being great teachers: George J. Moridis, Akhil Datta-Gupta, Eduardo Gildin, Charles Glover, Frank Sottile, Joseph E. Pasciak, Wolfgang Bangerth, Raytcho Lazarov, Roger Smith, Jon Pitts and Thomas Schlumprecht. Their courses greatly inspired me and formed the foundation for this dissertation.

Finally, many thanks to my family for their endless love and support.

CONTRIBUTORS AND FUNDING SOURCES

Contributors

This work was supported by a dissertation committee consisting of Professor John E. Killough [advisor], Professor Eduardo Gildin and Professor Hadi Nasrabadi of the Department of Petroleum Engineering and Professor Maria A. Barrufet of the Department of Chemical Engineering.

The geological structures depicted in Chapter 5 were prepared by Dr. Mohamed M. Fadlelmula F. of the Department of Petroleum Engineering at Texas A&M University at Qatar in several co-authored articles listed in the Biographical Sketch.

All other work conducted for the dissertation was completed by the student independently. Portions of this research were conducted with high performance research computing resources provided by Texas A&M University (http://hprc.tamu.edu).

Funding Sources

This dissertation was made possible by the NPRP award [NPRP 6-485-2-201] from the Qatar National Research Fund (a member of The Qatar Foundation). The statements made herein are solely the responsibility of the authors.

NOMENCLATURE

Physical Quantities:

c_o	compressibility, Pa^{-1}
g	earth gravity, m/s^2
m	mass production rate, kg/s
$\dot{m}$	mass injection rate per unit volume, $kg/m^3/s$
p	pressure, Pa
t	time, s
u	velocity, m/s
T	temperature, K
WI	well index, $kg/s/Pa$
μ	fluid viscosity, $Pa \cdot s$
μ^*	effective viscosity of the fluid, $Pa \cdot s$
ρ	fluid density, kg/m^3
ϕ	porosity

Grid and Computation:

h	perturbation
A	face area of the grid block, m^2
R	Jacobian function
N	number of grid blocks, total or in a subscripted direction
R	residual function
V	volume of the grid block, m^3

X	independent variable, can be pressure or velocity
ϵ	tolerance
Δt	time step size, s
Δx	spacing in the x-direction, m
Δy	spacing in the y-direction, m
Δz	spacing in the z-direction, m

Vectors and Tensors:

$\mathbf{g}$	gravity vector, m^2/s
$\mathbf{k}$	permeability tensor, m^2
$\mathbf{p}$	pressure vector, Pa
$\mathbf{u}$	velocity vector, m/s
$\mathbf{J}$	Jacobian matrix
$\mathbf{R}$	residual vector
$\mathbf{X}$	independent variable vector
$\mathbf{\Delta}$	update vector

Superscripts and Subscrpits:

x, y, z	Cartesian coordinates
i, j, k	indices of the grid block
l, m	indices of vectors and matrices
n	number of time steps
bh	bottomhole
ic	initial conditions
f	fractures and karsts
m	porous media

ref	reference
ν	iteration number

Abbreviations:

GMRES	generalized minimal residual method
BFGS	Broyden-Fletcher-Goldfarb-Shanno method
DFVN	Discrete Fracture-Vug Networks
MPG	Multiple-Point Geostatistics
SNESIM	Single Normal Equation Simulation
SGeMS	Stanford Geostatistical Modeling Software

TABLE OF CONTENTS

Page

LIST OF FIGURES

FIGURE Page

LIST OF TABLES

TABLE Page

1. INTRODUCTION*

1.1 Carbonate Reservoirs: A Global Perspective

Carbonate reservoirs are commonly found across the world. Figure 1.1 displays the world-wide geographic distributions of carbonate reserves and carbonate oil provinces. From the numbers on the graph it is readily estimated that more than 60% of the world's proved oil reserves were held in carbonates in 2006. In particular, according to BP Statistical Review 2016 [2], the Middle East held around 55% of the world's proved oil reserves and 46% of the world's proved natural gas reserves in 2005. Approximately 70% of these oil reserves and 90% of these gas reserves are kept in carbonate reservoirs [1], netting to about 39% and 41% of the world's proved oil and gas reserves, respectively. These numbers dropped gradually over the past ten years due to the rapid development of unconventional oil and gas resources, but as shown in Figures 1.2 and 1.3, the Middle East alone still held approximately 47% of the world's proved oil reserves and 43% of the world's proved natural gas reserves in 2015, netting to about 33% and 39% of the world's proved oil and gas reserves, respectively. Behind these numbers it is clear that carbonate reservoirs play a significant role in today's global energy market, and they will continue to do so despite the development of shales and other unconventional resources, given the vast fields of deep water carbonates that we have yet to explore.

*Part of this section is reprinted with permission from "A Unified Finite Difference Model for The Simulation of Transient Flow in Naturally Fractured Carbonate Karst Reservoirs" by J. He, J. E. Killough, M. M. Fadlelmula F., and M. Fraim, 2015. SPE Proceedings, Copyright [2017] by Society of Petroleum Engineers.

1.2 The Basic Geological Principles

Many theories have been developed by geologists to understand the formation and characterization of carbonate reservoirs. Among them stands the carbonate factory theory and Dunham's carbonate classification. Dunham proposed in 1960 [3] that we can classify carbonate rocks into limestone and crystalline, with the former divided into mud-

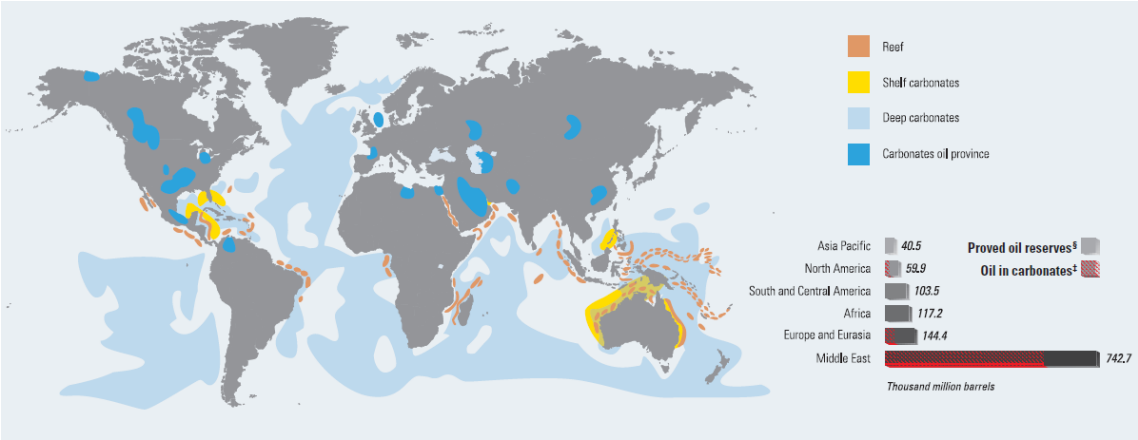

Figure 1.1: World distribution of carbonate reserves and carbonate oil provinces [1].

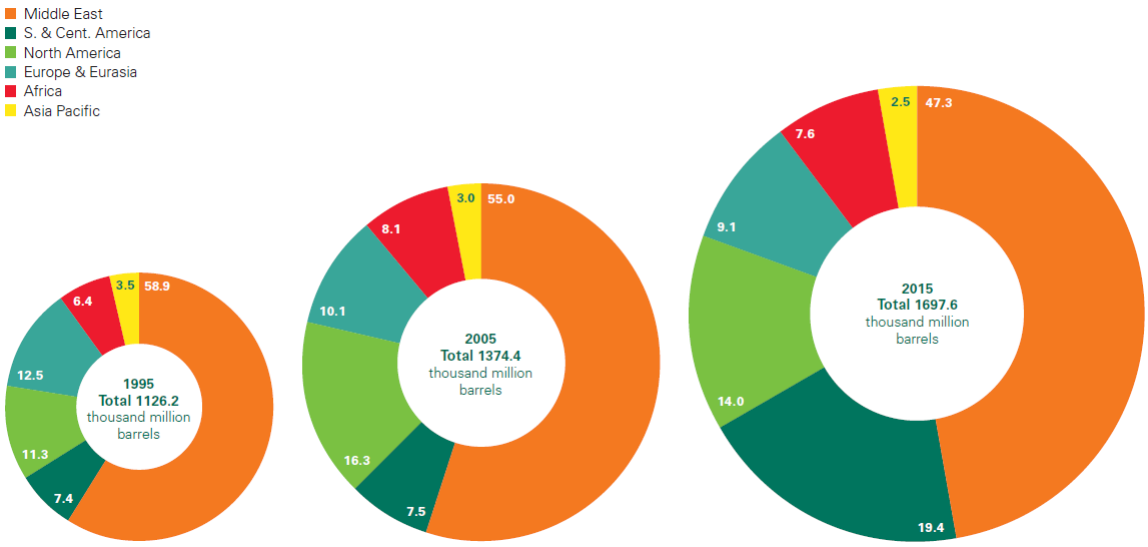

Figure 1.2: Distribution of proved oil reserves by region in 1995, 2005 and 2015 [2].

stone, wackstone, packstone, grainstone and boundstone based on their texture, as shown in Figure 1.4. It was not until 2005 that the carbonate factory theory was first defined by Schlager [14]. The theory describes the precipitation and sedimentation of carbonate minerals in shallow sea and how the carbonates are transported towards the shore and deep sea, respectively (Figure 1.5).

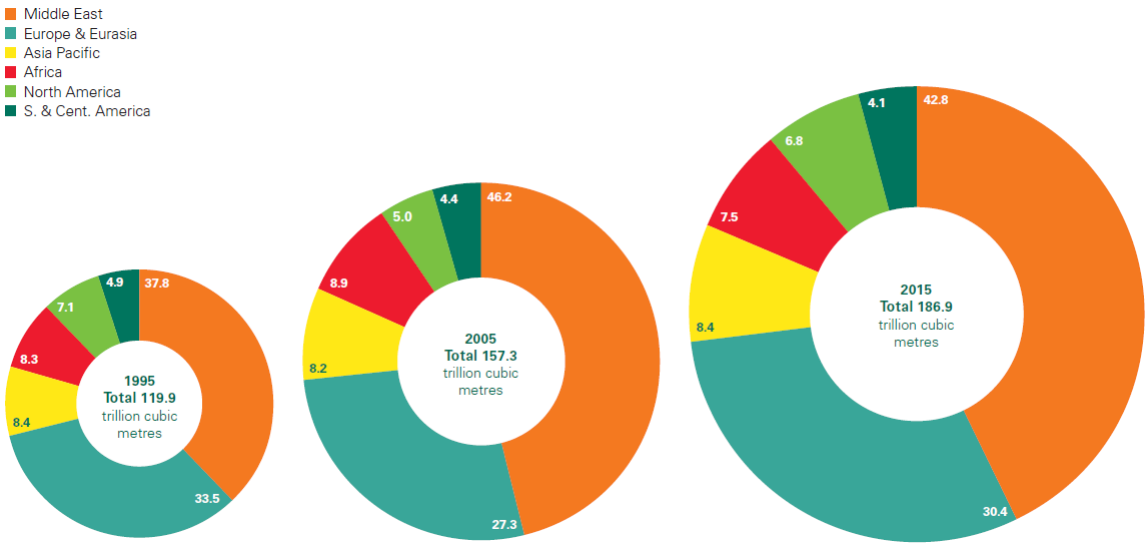

Figure 1.3: Distribution of proved natural gas reserves by region in 1995, 2005 and 2015 [2].

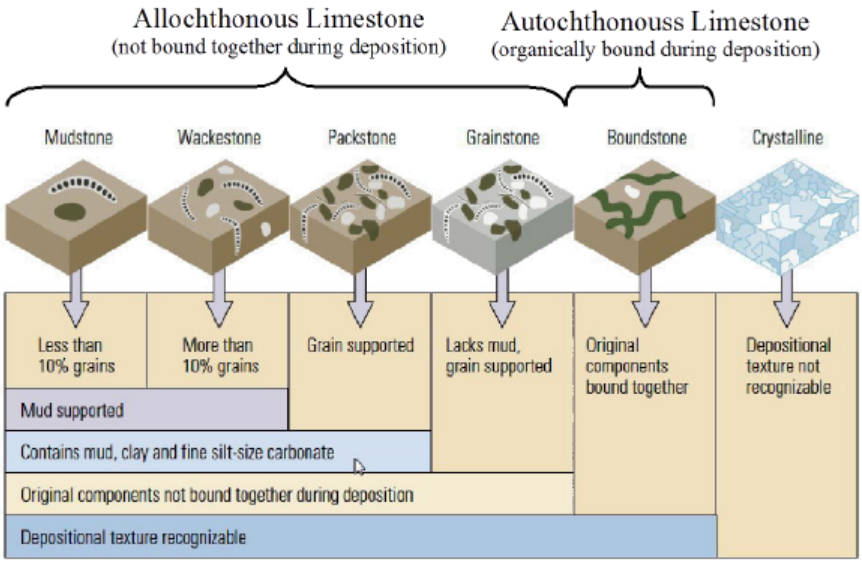

Figure 1.4: Carbonate rock classification [3].

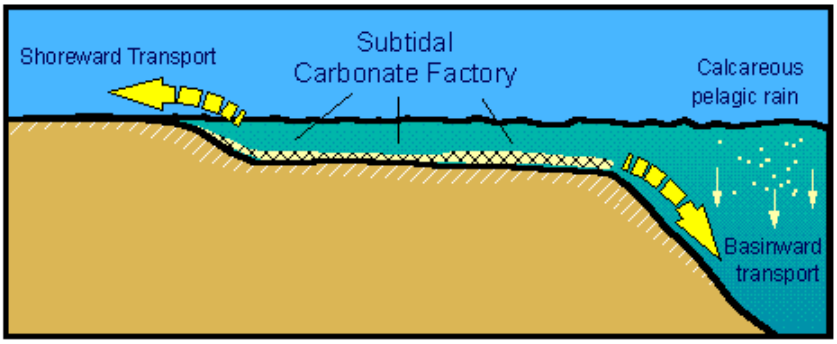

Figure 1.5: Carbonate factory theory [4].

1.3 Porosity Development and Classfication

Carbonate reservoirs are notorious for their high heterogeneity. Detailed classifications of carbonate porosity types are difficult yet available, like the one proposed by Choquette and Pray [5], which divides carbonate porosity into three broad categories, i.e. frabric selective, not fabric selective, and fabric selective or not. Each category has some subdivisions as shown in Figure 1.6. While such a complex porosity classification is deemed meaningful for understanding the geological developments of different carbonate formations, it is usually an overkill for engineering applications. From an engineer's perspective, we will follow Dr. Wayne M. Ahr [6], who classifies carbonate porosity as primary and secondary porosity types (Figure 1.7). The primary porosity is the interparticle and intraparticle porosity at the microscopic level, with a diameter way less than $1mm$. The secondary porosity includes vugs and caves which are diagenetic porosity resulting from chemical changes like dissolution and displacement, and natural fractures which come from mechanical processes like compaction and distortion [15, 16]. The small vugs and large caves are collectively known as karst porosity, with diameters ranging from millimeters to meters. The natural fractures usually has widths less than $1mm$ and lengths as long

as $1km$.

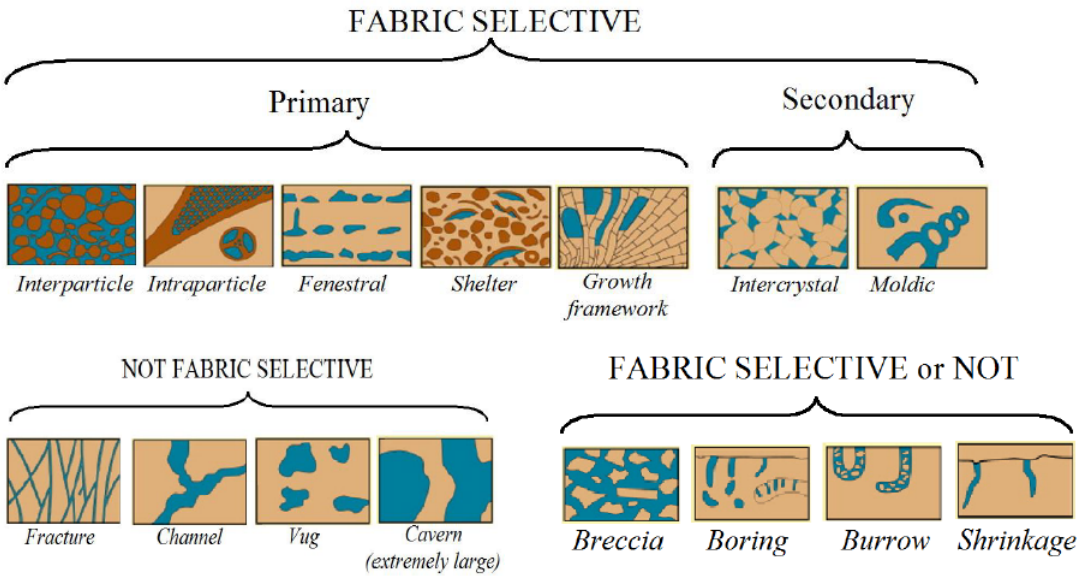

Figure 1.6: Carbonate porosity classification by Choquette and Pray [5].

1.4 Mathematical Models for Fluid Flow in Carbonate Reservoirs

Fluid flow in the macroscopic pore spaces cannot be simply assumed as a linear function of pressure gradient [7], so that the application of Darcy's law to predicting hydrocarbon production in such highly heterogeneous reservoirs becomes questionable and often yields unsatisfactory results. Figure 1.8 clearly illustrates the deviation from Darcy law when Reynolds number is larger than one. Considering that the plot is in logarithmic scale, the differences are more significant than depicted.

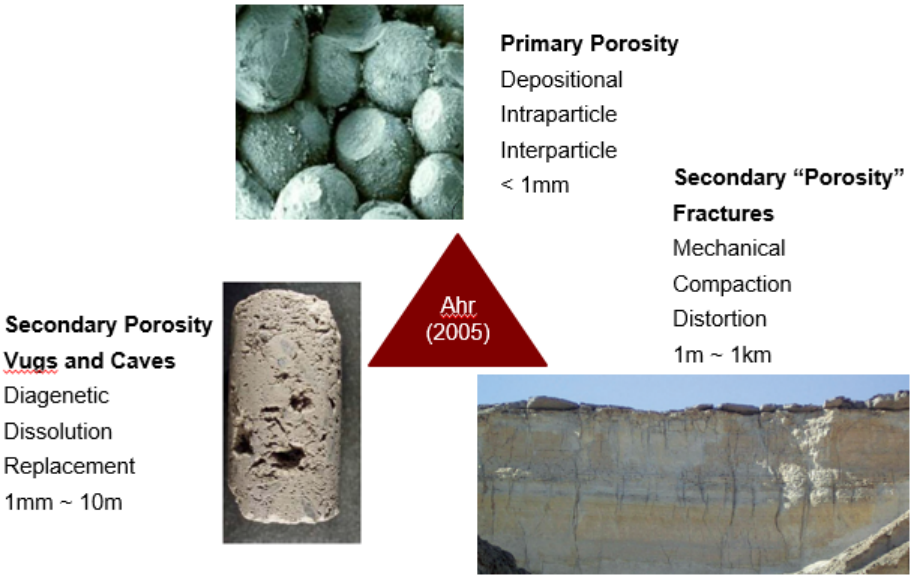

Figure 1.7: Porosity types in carbonate reservoirs [6].

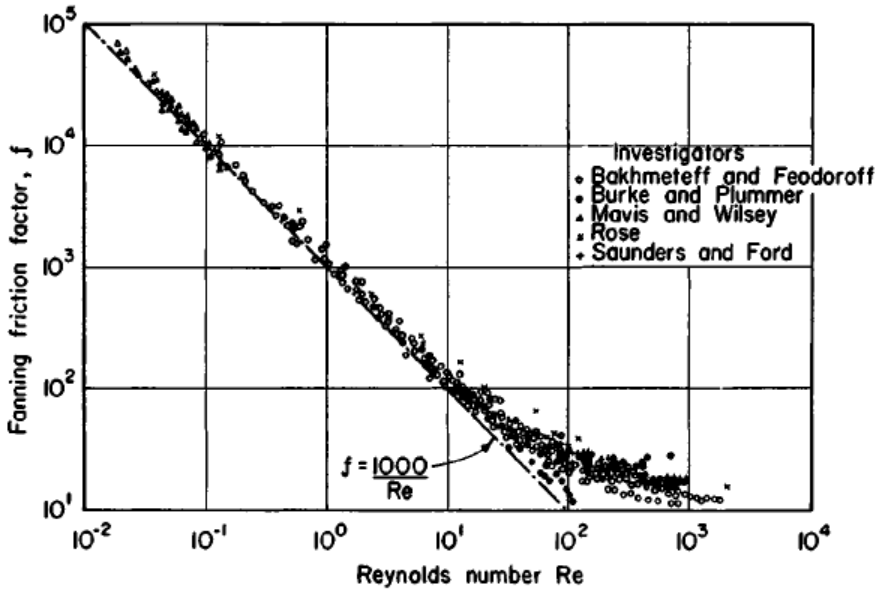

Figure 1.8: Relationship between Fanning's friction factor and Reynolds number for flow through granular porous media [7].

In short, the modeling and numerical simulation of the coupled fluid flow in naturally fractured carbonate karst reservoirs are extremely challenging due to non-Darcy flow in vugs and caves connected by fracture networks [17, 18], and deserve more efforts and better ideas from both the engineering and computational sides [19]. Many models have been developed in the past decade for the simulation of fluid flow in a naturally fractured reservoir and for carbonate karst reservoirs. We would like to summarize the major types in this section.

1.4.1 Extended Darcy Models

Various continuum approaches have been developed for the modeling of fluid flow in naturally fractured carbonate karst reservoirs. Methods based on the multiple-continuum concept model fractures and vugs as porous media with high permeability values [20, 21, 22, 23, 24, 25, 26, 27, 28, 29, 30, 31]. These methods are also widely applied in the simulation of hydraulically fractured unconventional reservoirs [32, 33, 34, 35, 36, 37] since hydraulic fractures are no different from natural fractures in terms of the type of fluid flow therein. Another continuum approach combines the porous media, fractures, and cavities together as a single effective porous medium [38, 39, 40], and use effective porosity and permeability to approximate the fluid storage and transport behavior in the fractured vuggy reservoirs. The continuum approaches have simple formulations and are computationally efficient, but the difficulty in estimating the cavity permeability or effective porosity/permeability values limit their applications in fractured carbonate karst reservoirs [41].

1.4.2 The Darcy-Stokes Model

Another approach for modeling fluid flow in fractured carbonate karst reservoirs is based on the Darcy-Stokes system [42, 43, 44, 41]. The Darcy-Stokes system consists of free flow in cavities and fractures characterized by Stokes equation and fluid flow in porous media by Darcy's Law. The coupled Darcy and Stokes equations are more difficult to solve, and additional boundary conditions [45, 46, 47] need to be specified at the interface between cavities and porous media to guarantee continuity of mass and momentum across the interface. The specification of such boundary conditions requires a fairly detailed knowledge of the location and extent of the interface which in turn makes the application of the Darcy-Stokes approach complicated [48].

1.4.3 The Stokes-Brinkman Model

The Stokes-Brinkman equation [8] provides a unified approach which avoids some of the problems encountered in the Darcy-Stokes system. This approach is unified in the sense that it uses a single equation rather than coupled ones to describe fluid flow in the entire fractured carbonate karst reservoir. The Stokes-Brinkman equation can be shown to be equivalent to the Darcy and Stokes equations [8, 49] once appropriate parameters are selected in the corresponding flow regions, respectively. Therefore, explicit modeling of the interface is avoided, allowing a seamless transition between the vugs and porous media [50, 51, 49].

Many papers are devoted to the numerical formulation and solution of the Stokes-Brinkman equation [52, 53, 50, 51, 54, 49, 48, 55, 56, 57, 58, 59], but to the best of our knowledge, all of them consider only steady-state flow, and are applied towards 2D streamline-based type of simulations. In this study, we propose a single-phase transient flow model for fluid transport in naturally fractured carbonate karst reservoirs [13, 10, 60].

This transient flow model consists of the Stokes-Brinkman equation, and a generalized material balance equation which is unsteady state and exact in the entire reservoir. Finite differences are implemented for the solution of the proposed transient flow model, which provides a smooth transition from standard multiple-porosity/permeability reservoir simulators. This solution method is physically more straightforward, easier to derive and implement, and proves more apt to generalization from 2D to 3D cases than alternative techniques. The derived transient flow model is applied to several fine-scale 2D and 3D geological models. The results of these models form the foundation for future study of multi-phase and multi-scale reservoir cases.

2. THE TRANSIENT STOKES-BRINKMAN MODEL

2.1 Flow Models for Different Regions of a Carbonate Reservoir

The solution of fluid flow problems, whether in porous media or not, generally starts from the homogenization of relevant conservation laws. In this section, a brief discussion is presented on the derivation of material and momentum balance equations for fluid flow in different regions of a naturally fractured carbonate karst reservoir. Here I strive for a thorough understanding of the physical assumptions underlying the derivation process, which largely determine the final forms of these equations as well as their range of geapplicability. These equations form the basis for all the numerical work in later chapters.

2.1.1 Flow in Carbonate Matrix

Single-phase fluid flow in the carbonate matrix, just like that in any porous media, is completely described by the material balance equation

$$\frac{\partial}{\partial t}(\phi\rho) + \nabla \cdot (\rho \mathbf{u}) = \dot{m} \tag{2.1}$$

and Darcy's law [61]

$$\mathbf{u} = -\frac{\mathbf{k}}{\mu}(\nabla p - \rho \mathbf{g}) \tag{2.2}$$

where ϕ and $\mathbf{k}$ are the porosity value and permeability tensor of the porous media, ρ and μ are fluid density and viscosity, $\mathbf{u}$ is the Darcy velocity vector, t is time, p is the average pore pressure, $\dot{m}$ is mass injection/production ($\pm$) rate per unit volume, and $\mathbf{g}$ is earth gravity vector [62]. As a convention, the permeability tensor $\mathbf{k}$ is usually assumed to be diagonal and anisotropic, on which the effect of pressure p is ignored in this study.

Equation 2.1 is derived with the method of homogenization, by relating the mass flow passing a control volumn to its internal mass change through the divergence theorem. Equation 2.2 was first formulated by Henry Darcy based on the results of a series of experiments on the 1D downflow of water through a vertical column of filter sands, and was published in the appendix of his book *Les fo ntain es Publiques de lu Ville de Dijon* in 1856 [63]. This equation soon became known as Darcy's law and has since been found valid for and applied to any Newtonian fluid flow in porous media. Moreover, although Equation 2.2 was established under saturated flow conditions, it has been extended and applied to unsaturated and multiphase flow [64] with tremendous success in the past century.

2.1.2 Flow in Fractures and Karst

Fractures, vugs and caves are no different from one another in the sense that they are all secondary porosity types at the macroscopic level. Single-phase fluid low on this scale is characterized by the continuity equation

$$\frac{D\rho}{Dt} + \rho\nabla \cdot \mathbf{u} = \frac{\partial \rho}{\partial t} + \nabla \cdot (\rho \mathbf{u}) = \dot{m} \tag{2.3}$$

and the equation of motion [65]

$$\rho \frac{D\mathbf{u}}{Dt} = -\nabla \cdot \boldsymbol{\tau} - \nabla p + \rho \mathbf{g} \tag{2.4}$$

where $\mathbf{u}$ is the true velocity vector which is physically different from the Darcy velocity in Equations 2.1 and 2.2, $\boldsymbol{\tau}$ is the total stress tensor, and the other variables are defined as before. The total stress tensor $\boldsymbol{\tau}$ is described by the constitutive equation [66]

$$\boldsymbol{\tau} = -\mu \left(\nabla \mathbf{u} + \nabla \mathbf{u}^T\right) + \left(\frac{2}{3}\mu - \kappa\right)(\nabla \cdot \mathbf{u})\,\mathbf{I} \tag{2.5}$$

where κ is the bulk viscosity coefficient, and $\mathbf{I}$ is the identity tensor. For Newtonian fluid, we can impose the Stokes hypothesis [67, 68]

$$\frac{2}{3}\mu - \kappa = 0 \tag{2.6}$$

In spite of the evidently weak physical justification of Equation 2.6, it has been applied to most compressible flows and yielded good results [67]. If we substitute Equation 2.6 into Equation 2.5, along with the assumption of constant fluid viscosity μ, and then apply the divergence operator $\nabla\cdot$ to both sides of the equation, we get

$$\nabla \cdot \boldsymbol{\tau} = -\mu \left(\Delta \mathbf{u} + \nabla \cdot \nabla \mathbf{u}^T\right) = -\mu \Delta \mathbf{u} \tag{2.7}$$

since $\nabla \cdot (\nabla \mathbf{u})^T \equiv 0$ [66]. Again we can substitute Equation 2.7 into Equation 2.4 to obtain the Navier-Stokes equation

$$\rho \frac{D\mathbf{u}}{Dt} = \mu \Delta \mathbf{u} - \nabla p + \rho \mathbf{g} \tag{2.8}$$

If we further assume steady state in the Lagrangian specification of the flow field, i.e. $D\mathbf{u}/Dt = 0$, where

$$\frac{D}{Dt} = \frac{\partial}{\partial t} + \mathbf{u} \cdot \nabla \tag{2.9}$$

then Equation 2.8 reduces to the Stokes equation

$$\mu \Delta \mathbf{u} - \nabla p + \rho \mathbf{g} = \mathbf{0} \tag{2.10}$$

Strictly speaking, Equation 2.10 holds only for incompressible Newtonian fluid of constant density and viscosity, where constant density comes in as an underlying assumption for Equation 2.4. However, these assumptions are usually freely exploited in numerical

simulation processes, in order to guarantee a precise material balance in Equation 2.3.

Coupling Equation 2.2 in carbonate matrix with Equation 2.10 in fractures and karst results in the so-called Darcy-Stokes model, which always entails additional interfacial boundary conditions and is thus difficult to solve. To avoid such difficulties, a unified formulation will be presented instead in the next section, which allows a seamless transition between different flow regions and is therefore easier to solve numerically.

2.2 The Stokes-Brinkman Model: A Unified Formulation

H.C. Brinkman, an engineer of Royal Dutch Shell, made an observation in 1949 [8] that, by introducing an extra factor, namely the "effective" fluid viscosity μ^*, Equations 2.2 and 2.10 can be combined into a unified formula, which is now known as the Brinkman equation, the Stokes-Brinkman equation, or the Darcy-Stokes-Brinkman equation

$$\mathbf{u} + \frac{\mathbf{k}}{\mu}\left(\nabla p - \rho \mathbf{g} - \mu^* \Delta \mathbf{u}\right) = \mathbf{0} \tag{2.11}$$

Equation 2.11 is mathematically equivalent to Equations 2.2 and 2.10 in the following manner: it reduces to Equation 2.2 if we set $\mu^* = 0$ in the carbonate matrix, and converges to Equation 2.10 if we let $\mathbf{k} \to \infty$ (or rather by applying very large permeability values to the fractures and karst regions) and $\mu^* = \mu$ in the fractured and karstic regions. Instead of treating μ^* differently in different flow regions, it is also feasible to approximate it uniformly throughout the carbonate reservoir. To do so, Mr. Brinkman paired Equation 2.11 with the steady-state material balance equation

$$\nabla \cdot \mathbf{u} = 0 \tag{2.12}$$

and solved them analytically. By comparing his analytical solutions to an experimetal

relationship developed by P.C. Carman [9] (see Figure 2.1, where η and η' denote μ and μ^*, respectively), he recommended to choose $\mu^* = \mu$ for all practical purposes. Compared to the former differential treatment, this uniform approximation only introduces a small perturbation into the numerical solutions [56], because $\mu^* \Delta \mathbf{u}$ is normally several orders of magnitude smaller than the other terms on the left side of Equation 2.11 in typical porous media [50]. Figure 2.2 shows that for the steady-state flow, pressure distributions and streamlines don't change much as μ^* decreases.

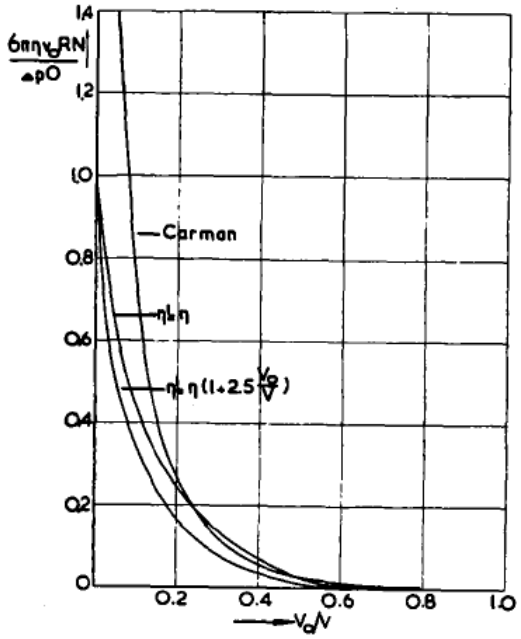

Figure 2.1: Comparison of Brinkman's analytical solutions to Carman's experimental results [8, 9].

The Stokes-Brinkman equation used to have limited applications since it was always paired with a material balance equation that presumes steady-state flow in the Eulerian specification, such as Equation 2.12. However, as can be seen from the derivation process

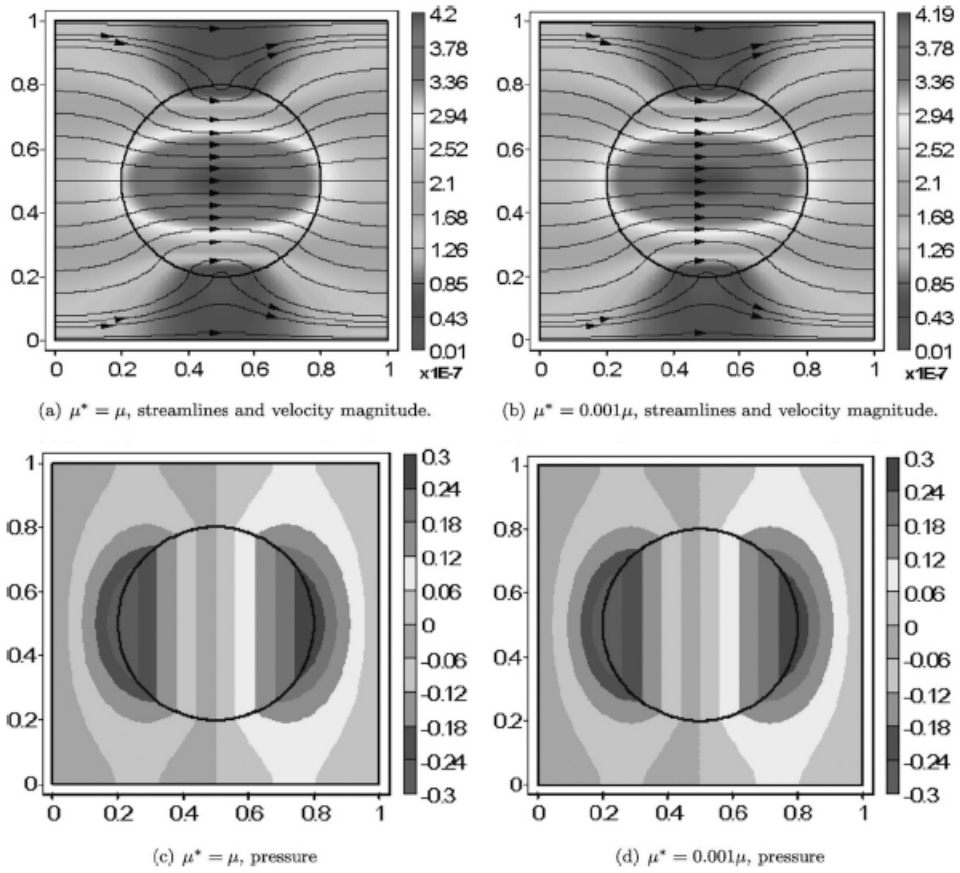

(a) $\mu^* = \mu$, streamlines and velocity magnitude. (b) $\mu^* = 0.001\mu$, streamlines and velocity magnitude.

(c) $\mu^* = \mu$, pressure (d) $\mu^* = 0.001\mu$, pressure

Figure 2.2: Effect of the term μ^* in the porous region of the Stokes-Brinkman equation*.

in the previous section, neither Darcy's law nor the Stokes equation makes such an assumption, so in theory the composite Stokes-Brinkman equation should also be applicable to transient flow, so we combine it with the transient material balance equation

$$\frac{\partial}{\partial t}(\phi\rho) + \nabla \cdot (\rho \mathbf{u}) = \dot{m} \tag{2.1}$$

to form the unified transient Stokes-Brinkman model, since, similar to Equation 2.11,

*Reprinted with permission from "Multiphysics and Multiscale Methods for Modeling Fluid Flow Through Naturally Fractured Carbonate Karst Reservoirs" by P. Popov, G. Qin, L. Bi, Y. Efendiev, R. E. Ewing, and J. Li, 2009. SPE Reservoir Evaluation & Engineering, Volume 12, Issue 2, Copyright [2017] by Society of Petroleum Engineers.

Equation 2.1 is unified in a sense that it not only describes the material balance for fluid flow in porous media, but can also be reduced to Equation 2.3 for flow in macroscopic porosities like fractures and karst, as long as we keep $\phi = 1$ in those regions. Consequently, Equation 2.1 is exact in the entire carbonate reservoir, even though the velocity vector $\mathbf{u}$ bears different physical meanings in different flow regions.

Again, the above proposed transient flow model consisting of Equations 2.1 and 2.11, as suggested by the underlying assumptions, is suitable only for incompressible fluid flow and should be extended with caution to slightly compressible fluids. For compressible gas flow, however, the gas slippage effect is significant, and Klinkenberg factor based [69, 70] or Knudsen's number based methods [32, 71] should be employed to modify the permeability tensor $\mathbf{k}$ in Equation 2.2. Moreover, we should no longer assume the material derivative term $D\mathbf{u}/Dt$ to be negligible as we did in Equation 2.11, but rather couple the full Navier-Stokes equation with a modified Darcy's law to characterize the momentum balance of gas flow in a fractured karst reservoir, for which the development of a unified model is significantly more difficult.

3. MODEL DISCRETIZATION

3.1 Derivation of the Fully-Implicit Finite Difference Methods

To solve a mathematical model involving differential equations, the first step is to find a discrete approximation that converges to the original model asymptotically. Since the Stokes-Brinkman equation is a vector equation, we have to in effect discretize the following four scalar equations for the transient Stokes-Brinkman model in the Cartesian coordinates:

$$\frac{\partial}{\partial t}(\phi\rho) + \frac{\partial}{\partial x}(\rho u_x) + \frac{\partial}{\partial y}(\rho u_y) + \frac{\partial}{\partial z}(\rho u_z) = \dot{m} \tag{3.1}$$

$$\mu u_x + k_x \left[\frac{\partial p}{\partial x} - \mu^* \left(\frac{\partial^2 u_x}{\partial x^2} + \frac{\partial^2 u_x}{\partial y^2} + \frac{\partial^2 u_x}{\partial z^2}\right)\right] = 0 \tag{3.2}$$

$$\mu u_y + k_y \left[\frac{\partial p}{\partial y} - \mu^* \left(\frac{\partial^2 u_y}{\partial x^2} + \frac{\partial^2 u_y}{\partial y^2} + \frac{\partial^2 u_y}{\partial z^2}\right)\right] = 0 \tag{3.3}$$

$$\mu u_z + k_z \left[\frac{\partial p}{\partial z} - \rho g - \mu^* \left(\frac{\partial^2 u_z}{\partial x^2} + \frac{\partial^2 u_z}{\partial y^2} + \frac{\partial^2 u_z}{\partial z^2}\right)\right] = 0 \tag{3.4}$$

where u_x, u_y, u_z are the velocities, and k_x, k_y, k_z the permeabilities in the corresponding directions, g is the gravity, and all the other variables are as previously defined. The gravity term $-\rho g$ only appears in Equation 3.4, because the z-direction is purposely aligned with the earth gravity/depth direction. If the z-direction is reversed, then the sign of the gravity term should also be reversed accordingly. In these four equations, p, u_x, u_y, u_z are the four variables that we need to solve for as functions of space and time. In the following subsections, we shall apply the fully-implicit finite difference method to discretize the four equations above, so that we can solve for the four variables numerically at discrete spatial

locations and time points.

3.1.1 A Naïve Approach

The block-centered finite difference method is employed for the discretization of the transient Stokes-Brinkman model on uniformly-sized staggered grids, as illustrated in Figure 3.1,

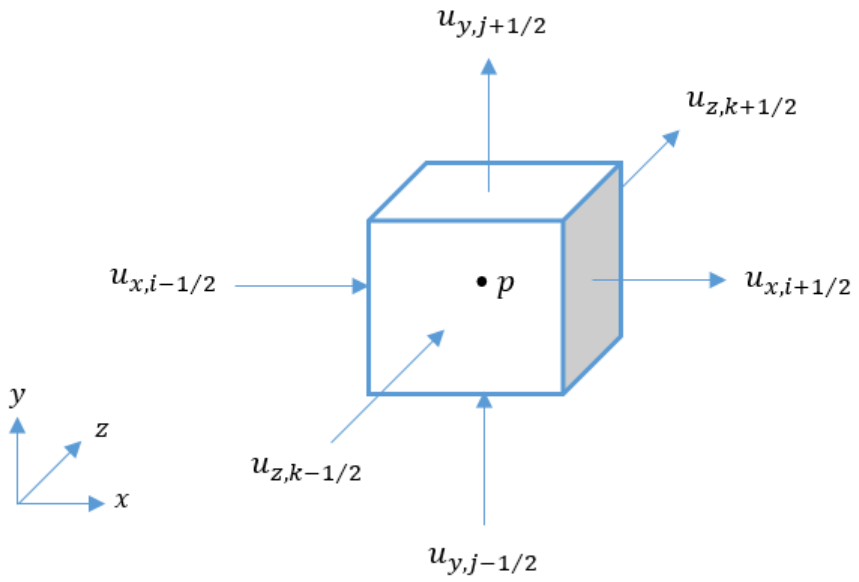

Figure 3.1: Definition of pressure and velocities for a block with index (i, j, k).

where we define pressure at the block center, and velocities at block interfaces as indicated by the subscripts $i \pm 1/2$, $j \pm 1/2$, and $k \pm 1/2$, which is equivalent to solving Equation 3.1 at all such block centers and Equations 3.2–3.4 at all such interfaces, respectively. It is very tempting at first glance to define pressure and velocities both at the block center, which, however, will actually break the material balance of the block, and introduce more numerical errors at the flow boundaries.

Formally, the subscripts of each variable in Figure 3.1 should contain its 3D Cartesian coordinates, i.e. p, $u_{x,i\pm1/2}$, $u_{y,j\pm1/2}$, and $u_{z,k\pm1/2}$ should be written as $p_{i,j,k}$, $u_{x,i\pm1/2,j,k}$, $u_{y,i,j\pm1/2,k}$, and $u_{z,i,j,k\pm1/2}$, respectively, but we prefer the simplier notations which make the finite difference equations look much more concise. We will adopt this notation simplification throughout the dissertation.

The basic idea of the finite difference method is to obtain an approximation for the partial derivative of a smooth function by employing the Taylor remainder theorem [72]. Let $f(x)$ be a smooth function, then the nth-order Taylor series of $f(x+\Delta x)$ is

$$\begin{aligned} f\left(x+\Delta x\right) =& \sum_{0}^{n} \frac{f^{(k)}\left(x\right)}{n!}\left(\Delta x\right)^{k} + \frac{f^{(n+1)}\left(\xi\right)}{(n+1)!}\left(\Delta x\right)^{(n+1)} \\ =& f\left(x\right) + f^{'}\left(x\right)\Delta x + \frac{f^{''}\left(x\right)}{2!}\left(\Delta x\right)^{2} + \cdots + \frac{f^{(n)}\left(x\right)}{n!}\left(\Delta x\right)^{n} \\ &+ \frac{f^{(n+1)}\left(\xi\right)}{(n+1)!}\left(\Delta x\right)^{(n+1)} \end{aligned} \tag{3.5}$$

for some $\xi \in [x, x+\Delta x]$. Take $n = 1, 2, 3$, respectively, and rearrange the terms, then Equation 3.5 becomes

$$f^{'}\left(x\right)\Delta x = f\left(x+\Delta x\right) - f\left(x\right) - \frac{f^{''}\left(\xi^{+}\right)}{2!}\left(\Delta x\right)^{2} \tag{3.6}$$

$$f^{'}\left(x\right)\Delta x = f\left(x+\Delta x\right) - f\left(x\right) - \frac{f^{''}\left(x\right)}{2!}\left(\Delta x\right)^{2} - \frac{f^{'''}\left(\eta^{+}\right)}{3!}\left(\Delta x\right)^{3} \tag{3.7}$$

$$f^{'}\left(x\right)\Delta x = f\left(x+\Delta x\right) - f\left(x\right) - \frac{f^{''}\left(x\right)}{2!}\left(\Delta x\right)^{2} - \frac{f^{'''}\left(x\right)}{3!}\left(\Delta x\right)^{3} - \frac{f^{(4)}\left(\zeta^{+}\right)}{4!}\left(\Delta x\right)^{4} \tag{3.8}$$

for some $\xi^{+}, \eta^{+}, \zeta^{+} \in [x, x+\Delta x]$. If we divide both sides of Equation 3.6 by Δx, then

we get the forward difference formula

$$\begin{aligned} f^{'}(x) &= \frac{f(x+\Delta x)-f(x)}{\Delta x} - \frac{f^{''}(\xi^{+})}{2!}\Delta x \\ &= \frac{f(x+\Delta x)-f(x)}{\Delta x} + O(\Delta x) \end{aligned} \tag{3.9}$$

where $O(\Delta x)$ denotes the first-oder local truncation error, i.e. any error with order of magnitude proportional to Δx. If we substitute $-\Delta x$ for Δx in Equations 3.7 and 3.8, then we have

$$f^{'}(x)\Delta x = f(x) - f(x-\Delta x) + \frac{f^{''}(x)}{2!}(\Delta x)^{2} - \frac{f^{'''}(\eta^{-})}{3!}(\Delta x)^{3} \tag{3.10}$$

$$f^{'}(x)\Delta x = f(x) - f(x-\Delta x) + \frac{f^{''}(x)}{2!}(\Delta x)^{2} - \frac{f^{'''}(x)}{3!}(\Delta x)^{3} + \frac{f^{(4)}(\zeta^{-})}{4!}(\Delta x)^{4} \tag{3.11}$$

for some $\eta^{-}, \zeta^{-} \in [x-\Delta x, x]$. Adding Equations 3.7 and 3.10 together results in the central difference formula

$$2f^{'}(x)\Delta x = f(x+\Delta x) - f(x-\Delta x) - \frac{f^{(''')}(\eta^{+}) + f^{(''')}(\eta^{-})}{3!}(\Delta x)^{3}$$

$$f^{'}(x) = \frac{f(x+\Delta x)-f(x-\Delta x)}{2\Delta x} + O\left((\Delta x)^{2}\right) \tag{3.12}$$

where $O\left((\Delta x)^{2}\right)$ denotes the second-oder local truncation error. If we instead subtract Equation 3.11 from Equation 3.8 and rearrange the terms, then we obtain the second-order finite difference formula

$$f^{''}(x)(\Delta x)^{2} = f(x+\Delta x) - 2f(x) + f(x-\Delta x) - \frac{f^{(4)}(\zeta^{+}) + f^{(4)}(\zeta^{-})}{4!}(\Delta x)^{4}$$

$$f^{'}(x) = \frac{f(x+\Delta x)-f(x-\Delta x)}{2\Delta x} + O\left((\Delta x)^{2}\right) \tag{3.13}$$

Now we can use Equations 3.9, 3.12 and 3.13 to discretize the transient Stokes-Brinkman model for a grid block indexed (i, j, k) between current and future time steps t_n and t_{n+1}. Applying the forward difference formula 3.9 to the temporal partial derivative term in Equation 3.1 yields

$$\frac{\partial}{\partial t}(\phi\rho) \approx \frac{(\rho\phi)^{n+1} - (\rho\phi)^n}{\Delta t} \tag{3.14}$$

where $(\rho\phi)^n = \rho\phi|_{t=t_n}$, $\Delta t = t_{n+1} - t_n$, and the equality only holds approximately because we have ignored the first-order error term. Moreover, in contrast to fixing the block size, an adaptive strategy is adopted in practice to adjust the time step size Δt on the fly, which is mostly based on the convergent performance of the simulation process at the current time step.

Furthermore, Equation 3.12 can be applied to the spatial partial derivative terms in Equation 3.1, e.g. we have

$$\frac{\partial}{\partial x}(\rho u_x) \approx \frac{(\rho u_x)_{i+1/2} - (\rho u_x)_{i-1/2}}{\Delta x} \tag{3.15}$$

where Δx is the block size in the x-direction. There is no "2" in the denominator because each block interface is only $\frac{1}{2}\Delta x$ away from the block center. Discretize Equation 3.1 in this way and multiply both sides of the equation by the block volume $V = \Delta x \Delta y \Delta z$, then we have

$$\begin{aligned} \frac{V}{\Delta t}\left[(\rho\phi)^{n+1} - (\rho\phi)^n\right] &+ \left[A_x(\rho u_x)_{i+1/2} - A_x(\rho u_x)_{i-1/2}\right]^{n+1} \\ &+ \left[A_y(\rho u_y)_{j+1/2} - A_y(\rho u_y)_{j-1/2}\right]^{n+1} \\ &+ \left[A_z(\rho u_z)_{k+1/2} - A_z(\rho u_z)_{k-1/2}\right]^{n+1} + m^{n+1} = 0 \end{aligned} \tag{3.16}$$

where $A_x = \Delta y \Delta z$, $A_y = \Delta x \Delta z$, and $A_z = \Delta x \Delta y$ are the block surface areas perpendicular to the subscripted directions, Δx, Δy, and Δz are spacings in the corresponding

directions, m is the local mass injection/production ($\mp$) rate, and the other variables are as previously defined. All terms from the spatial derivatives have superscript $n+1$ rather than n, so that Equation 3.16 is a fully-implicit formulation.

Similarly, we can multiply apply Equation 3.12 to discretize the first-order partial derivatives and Equation 3.13 to the second-order ones in Equations 3.2–3.4 at block interfaces indexed with $(i+1/2, j, k)$, $(i, j+1/2, k)$, $(i, j, k+1/2)$, respectively. This time we shall multiply the three equations by $A_x\rho/\mu$, $A_y\rho/\mu$, $A_z\rho/\mu$ before discretizing them, and rearrange the terms afterwards, so that we get

$$\begin{aligned}
&A_x\left(\rho u_x\right)_{i+1/2} + \left(k_x\frac{\rho}{\mu}\right)_{i+1/2}\frac{A_x}{\Delta x}\left(p_{i+1}-p_i\right) \\
&\quad - \left(k_x\rho\frac{\mu^*}{\mu}\right)_{i+1/2}\frac{A_x}{\left(\Delta x\right)^2}\left(u_{x,i+3/2}-2u_{x,i+1/2}+u_{x,i-1/2}\right) \\
&\quad - \left(k_x\rho\frac{\mu^*}{\mu}\right)_{i+1/2}\frac{A_x}{\left(\Delta y\right)^2}\left(u_{x,i+1/2,j+1}-2u_{x,i+1/2}+u_{x,i+1/2,j-1}\right) \\
&\quad - \left(k_x\rho\frac{\mu^*}{\mu}\right)_{i+1/2}\frac{A_x}{\left(\Delta z\right)^2}\left(u_{x,i+1/2,k+1}-2u_{x,i+1/2}+u_{x,i+1/2,k-1}\right) \\
&\quad = 0
\end{aligned} \tag{3.17}$$

$$\begin{aligned}
&A_y\left(\rho u_y\right)_{j+1/2} + \left(k_y\frac{\rho}{\mu}\right)_{j+1/2}\frac{A_y}{\Delta y}\left(p_{j+1}-p_j\right) \\
&\quad - \left(k_y\rho\frac{\mu^*}{\mu}\right)_{j+1/2}\frac{A_y}{\left(\Delta x\right)^2}\left(u_{y,i+1,j+1/2}-2u_{y,j+1/2}+u_{y,i-1,j+1/2}\right) \\
&\quad - \left(k_y\rho\frac{\mu^*}{\mu}\right)_{j+1/2}\frac{A_y}{\left(\Delta y\right)^2}\left(u_{y,j+3/2}-2u_{y,j+1/2}+u_{y,j-1/2}\right) \\
&\quad - \left(k_y\rho\frac{\mu^*}{\mu}\right)_{j+1/2}\frac{A_y}{\left(\Delta z\right)^2}\left(u_{y,j+1/2,k+1}-2u_{y,j+1/2}+u_{y,j+1/2,k-1}\right) \\
&\quad = 0
\end{aligned} \tag{3.18}$$

$$
\begin{aligned}
A_z\left(\rho u_z\right)_{k+1/2} &+ \left(k_z\frac{\rho}{\mu}\right)_{k+1/2}\left[\frac{A_z}{\Delta z}\left(p_{k+1}-p_k\right)-A_z\rho_{k+1/2}g\right] \\
&- \left(k_z\rho\frac{\mu^*}{\mu}\right)_{k+1/2}\frac{A_z}{\left(\Delta x\right)^2}\left(u_{z,i+1,k+1/2}-2u_{z,k+1/2}+u_{z,i-1,k+1/2}\right) \\
&- \left(k_z\rho\frac{\mu^*}{\mu}\right)_{k+1/2}\frac{A_z}{\left(\Delta y\right)^2}\left(u_{z,j+1,k+1/2}-2u_{z,k+1/2}+u_{z,j-1,k+1/2}\right) \\
&- \left(k_z\rho\frac{\mu^*}{\mu}\right)_{k+1/2}\frac{A_z}{\left(\Delta z\right)^2}\left(u_{z,k+3/2}-2u_{z,k+1/2}+u_{z,k-1/2}\right) \\
&= 0
\end{aligned}
\tag{3.19}
$$

These equations are implicitly formulated even though the superscript $n+1$ is omitted for brevity. At each block interface, the permeability value is computed as the harmonic average of the permeability values of the two neighboring blocks, while fluid density ρ and viscosity μ are estimated by single-point upstream weighting or upwinding, i.e. by taking their values from the grid block that has a higher hydraulic head than its neighbor, so as to guarantee precise mass conservation across the grid blocks. For instance, we can take

$$
\frac{1}{k_{x,i+1/2}}=\frac{1}{k_{x,i}}+\frac{1}{k_{x,i+1}} \tag{3.20}
$$

$$
\rho_{x,i+1/2}=max\left(\rho_{x,i},\rho_{x,i+1}\right) \tag{3.21}
$$

Alternatively, fluid density ρ and viscosity μ can also be estimated by arithmetic averaging, which is slightly simplier than upstream weighting, and works almost equally well in practice.

3.1.2 Change of Variables

The finite different method displayed in the previous subsection is called naive or rather intuitive because we directly apply the first- and second-order difference formulas to Equa-

tions 3.1–3.4 without a moment's thought about possible transformations of the variables. In fact, an apparent problem with Equations 3.16–3.19 is that their forms are so complicated that numerical simulation of large geological models based on them can take from hours to days, which is not very computationally efficient. It turns out that a better idea is to substitute velocity u with mass flow rate F, so that Equations 3.1–3.4 can be subsequently reformulated, again by multiplying them with V, $A_x\rho/\mu$, $A_y\rho/\mu$, $A_z\rho/\mu$, respectively, as below:

$$V\frac{\partial}{\partial t}(\phi\rho) + \Delta x\frac{\partial F_x}{\partial x} + \Delta y\frac{F_y}{\partial y} + \Delta z\frac{F_z}{\partial z} + m = 0 \tag{3.22}$$

$$F_x + k_x A_x\frac{\rho}{\mu}\frac{\partial p}{\partial x} - k_x\frac{\mu^*}{\mu}\left(\frac{\partial^2 F_x}{\partial x^2} + \frac{\partial^2 F_x}{\partial y^2} + \frac{\partial^2 F_x}{\partial z^2}\right) = 0 \tag{3.23}$$

$$F_y + k_y A_y\frac{\rho}{\mu}\frac{\partial p}{\partial y} - k_y\frac{\mu^*}{\mu}\left(\frac{\partial^2 F_y}{\partial x^2} + \frac{\partial^2 F_y}{\partial y^2} + \frac{\partial^2 F_y}{\partial z^2}\right) = 0 \tag{3.24}$$

$$F_z + k_z A_z\frac{\rho}{\mu}\left(\frac{\partial p}{\partial z} - \rho g\right) - k_z\frac{\mu^*}{\mu}\left(\frac{\partial^2 F_z}{\partial x^2} + \frac{\partial^2 F_z}{\partial y^2} + \frac{\partial^2 F_z}{\partial z^2}\right) = 0 \tag{3.25}$$

where $F_x = A_x\rho u_x$, $F_y = A_y\rho u_y$, and $F_z = A_z\rho u_z$. Another subtle point is that by transforming Equations 3.2–3.4 to Equations 3.23–3.25, $\rho A_x\partial^2 u_x/\partial x^2$ is replaced with $\partial^2 F_x/\partial x^2$, $\rho A_y\partial^2 u_y/\partial y^2$ with $\partial^2 F_y/\partial y^2$ and so on, which in effect lifts the assumption of constant fluid density from the Stokes equation and improves the momentum balance. Now we can discretize Equations 3.22–3.25 which yields

$$\begin{aligned}\frac{V}{\Delta t}\left(\rho^{n+1}\phi^{n+1} - \rho^n\phi^n\right) &+ \left[F_{x,i+1/2} - F_{x,i-1/2}\right]^{n+1} \\ &+ \left[F_{y,j+1/2} - F_{y,j-1/2}\right]^{n+1} \\ &+ \left[F_{z,k+1/2} - F_{z,k-1/2}\right]^{n+1} + m^{n+1} = 0\end{aligned} \tag{3.26}$$

$$
\begin{aligned}
&F_{x,i+1/2} + \left(k_x \frac{\rho}{\mu}\right)_{i+1/2} \frac{A_x}{\Delta x} \left(p_{i+1} - p_i\right) \\
&\quad - \left(k_x \frac{\mu^*}{\mu}\right)_{i+1/2} \frac{1}{(\Delta x)^2} \left(F_{x,i+3/2} - 2F_{x,i+1/2} + F_{x,i-1/2}\right) \\
&\quad - \left(k_x \frac{\mu^*}{\mu}\right)_{i+1/2} \frac{1}{(\Delta y)^2} \left(F_{x,i+1/2,j+1} - 2F_{x,i+1/2} + F_{x,i+1/2,j-1}\right) \\
&\quad - \left(k_x \frac{\mu^*}{\mu}\right)_{i+1/2} \frac{1}{(\Delta z)^2} \left(F_{x,i+1/2,k+1} - 2F_{x,i+1/2} + F_{x,i+1/2,k-1}\right) \\
&\quad = 0
\end{aligned}
\tag{3.27}
$$

$$
\begin{aligned}
&F_{y,j+1/2} + \left(k_y \frac{\rho}{\mu}\right)_{j+1/2} \frac{A_y}{\Delta y} \left(p_{j+1} - p_j\right) \\
&\quad - \left(k_y \frac{\mu^*}{\mu}\right)_{j+1/2} \frac{1}{(\Delta x)^2} \left(F_{y,i+1,j+1/2} - 2F_{y,j+1/2} + F_{y,i-1,j+1/2}\right) \\
&\quad - \left(k_y \frac{\mu^*}{\mu}\right)_{j+1/2} \frac{1}{(\Delta y)^2} \left(F_{y,j+3/2} - 2F_{y,j+1/2} + F_{y,j-1/2}\right) \\
&\quad - \left(k_y \frac{\mu^*}{\mu}\right)_{j+1/2} \frac{1}{(\Delta z)^2} \left(F_{y,j+1/2,k+1} - 2F_{y,j+1/2} + F_{y,j+1/2,k-1}\right) \\
&\quad = 0
\end{aligned}
\tag{3.28}
$$

$$
\begin{aligned}
&F_{z,k+1/2} + \left(k_z \frac{\rho}{\mu}\right)_{k+1/2} \left[\frac{A_z}{\Delta z} \left(p_{k+1} - p_k\right) - A_z \rho_{k+1/2} g\right] \\
&\quad - \left(k_z \frac{\mu^*}{\mu}\right)_{k+1/2} \frac{1}{(\Delta x)^2} \left(F_{z,i+1,k+1/2} - 2F_{z,k+1/2} + F_{z,i-1,k+1/2}\right) \\
&\quad - \left(k_z \frac{\mu^*}{\mu}\right)_{k+1/2} \frac{1}{(\Delta y)^2} \left(F_{z,j+1,k+1/2} - 2F_{z,k+1/2} + F_{z,j-1,k+1/2}\right) \\
&\quad - \left(k_z \frac{\mu^*}{\mu}\right)_{k+1/2} \frac{1}{(\Delta z)^2} \left(F_{z,k+3/2} - 2F_{z,k+1/2} + F_{z,k-1/2}\right) \\
&\quad = 0
\end{aligned}
\tag{3.29}
$$

This new formulation consisting of Equations 3.26–3.29 is better than the old one of Equa-

tions 3.16–3.19 in many ways. First, velocity u, fluid density ρ, and cross-sectional area A are incorporated into one single term in the new formulation, namely mass flow F. This incorporation not only simplifies the appearance of the finite difference schemes, as is most clear if you compare Equation 3.16 with Equation 3.26, but also greatly reduces the number of multiplication operations to be performed at each time step, which in turn improves the computational efficiency of our simulator. Second, since the fluid density ρ is absorbed into the mass flow F at most places, we don't have to use the estimated ρ at grid block interfaces (where we have $\pm 1/2$ in the subscripts) as often as we did in the old formulation, resulting in an improvement of the accuracy of the finite-difference discretization. Third, the choice of mass flow rather than velocity is more natural in engineering applications, and is consistent with the convention in commercial multiple-porosity/permeability reservoir simulators. Last but not least, as we share soon see in the following section, the new formulation has better numerical properties than the old one, which is crucial for the convergence of the simulation results.

3.2 Convergence of Finite Differences: Theories and Implications

Now that we have two sets of numerical formulations of the transient Stokes-Brinkman model, we would like to assess their convergence properties. In particular, we would like to know if the numerical solutions of these formulations are close enough to the true solution of the analytical model, and if we have the numerical tools to solve the equations correctly. The former question is related to the convergence properties of the finite difference method we have used in those formulations, while the latter is related to the properties of the resulting linear system. We will discuss the convergence of the finite difference method in the subsequent sections, and postpone the discussion of the construction and properties of the linear system and the numerical methods to the next chapter.

The classic tool for proving the convergence of a numerical approximation method is the Lax-Richtmyer equivalence theorem [73], also called the fundamental theorem of numerical analysis, which can be stated loosely as follows:

Theorem 1 (Lax-Richtmyer)**.** *For a numerical approximation method for partial differential equations,*

$$\textit{consistency} + \textit{stability} = \textit{convergence}$$

where consistency means that the local truncation errors of the method decrease proportionally to some order of the block size, and stability means that the sizes of these errors are always uniformly bounded as they are passed through the time steps during the iterative process. A rigorous treatment of these definitons can be found in the classic textbook *Numerical Analysis: Mathematics of Scientific Computing* [74].

The finite difference formulations can be easily shown to be consistent with local truncation errors of second-order accuracy in space and first-order accuracy in time. Take the method represented by Equations 3.16–3.19 for instance. The proof is another typical application of the Taylor remainder theorem, or rather a direct application of the Equations 3.9, 3.12 and 3.13. First we apply Equations 3.9 and 3.12 to the material balance equation

3.1 at a block indexed (i, j, k), which results in

$$\begin{aligned}
&\frac{(\rho\phi)^{n+1} - (\rho\phi)^{n}}{\Delta t} + \frac{\Delta t}{2}\frac{\partial^2}{\partial x^2}(\rho\phi)^{n+} \\
&+ \frac{\left[(\rho u_x)_{i+1/2} - (\rho u_x)_{i-1/2}\right]^{n+1}}{\Delta x} - \frac{(\Delta x)^2}{48}\left[\frac{\partial^3}{\partial x^3}(\rho u_x)_{i+} + \frac{\partial^3}{\partial x^3}(\rho u_x)_{i-}\right] \\
&+ \frac{\left[(\rho u_y)_{j+1/2} - (\rho u_y)_{j-1/2}\right]^{n+1}}{\Delta y} - \frac{(\Delta y)^2}{48}\left[\frac{\partial^3}{\partial y^3}(\rho u_y)_{j+} + \frac{\partial^3}{\partial y^3}(\rho u_y)_{j-}\right] \\
&+ \frac{\left[(\rho u_z)_{k+1/2} - (\rho u_z)_{k-1/2}\right]^{n+1}}{\Delta z} - \frac{(\Delta z)^2}{48}\left[\frac{\partial^3}{\partial z^3}(\rho u_z)_{k+} + \frac{\partial^3}{\partial z^3}(\rho u_z)_{k-}\right] \\
&+ m^{n+1} = 0
\end{aligned} \tag{3.30}$$

where $\partial^2(\rho\phi)^{n+}/\partial x^2$, $\partial^3(\rho u_x)_{i\pm}/\partial x^3$, $\partial^3(\rho u_y)_{j\pm}/\partial y^3$, and $\partial^3(\rho u_z)_{k\pm}/\partial z^3$ are finite derivatives taken around the block center (i, j, k) and time point t_{n+1}, of which the exact locations and values are irrelevant to our proof. Now the local truncation error $\tau_{p,n+1}$ can be obtained by dividing Equation 3.16 by V and then subtracting it from Equation 3.30:

$$\begin{aligned}
\tau_{p,n+1} = \frac{\Delta t}{2}\frac{\partial^2}{\partial x^2}(\rho\phi)^{n+} &- \frac{(\Delta x)^2}{48}\left[\frac{\partial^3}{\partial x^3}(\rho u_x)_{i+} + \frac{\partial^3}{\partial x^3}(\rho u_x)_{i-}\right] \\
&- \frac{(\Delta y)^2}{48}\left[\frac{\partial^3}{\partial y^3}(\rho u_y)_{j+} + \frac{\partial^3}{\partial y^3}(\rho u_y)_{j-}\right] \\
&- \frac{(\Delta z)^2}{48}\left[\frac{\partial^3}{\partial z^3}(\rho u_z)_{k+} + \frac{\partial^3}{\partial z^3}(\rho u_z)_{k-}\right]
\end{aligned} \tag{3.31}$$

Take the inifity norm over the entire reservoir and between two time steps, and then apply the triangle inequality, so that

$$
\begin{aligned}
\left\|\tau_{p,n+1}\right\|_{\infty} \leq & \left\|\frac{1}{2}\frac{\partial^2}{\partial x^2}\left(\rho\phi\right)\right\|_{\infty}\Delta t + \frac{(\Delta x)^2}{24}\left\|\frac{\partial^3}{\partial x^3}\left(\rho u_x\right)\right\|_{\infty} \\
& + \frac{(\Delta y)^2}{24}\left\|\frac{\partial^3}{\partial y^3}\left(\rho u_y\right)\right\|_{\infty} + \frac{(\Delta z)^2}{24}\left\|\frac{\partial^3}{\partial z^3}\left(\rho u_z\right)\right\|_{\infty} \\
\leq & C_t\Delta t + C_p H^2
\end{aligned}
\tag{3.32}
$$

where

$$
\begin{aligned}
H &= max(\Delta x, \Delta y, \Delta z) \\
C_t &= \frac{1}{2}\left\|\frac{\partial^2}{\partial x^2}\left(\rho\phi\right)\right\|_{\infty} \\
C_p &= \frac{1}{24}\left\|\frac{\partial^3}{\partial x^3}\left(\rho u_x\right) + \frac{\partial^3}{\partial y^3}\left(\rho u_y\right) + \frac{\partial^3}{\partial z^3}\left(\rho u_z\right)\right\|_{\infty}
\end{aligned}
$$

Inequality 3.32 shows that Equation 3.16 is second-order accurate in space and first-order accurate in time. Similarly, we could show that Equations 3.17–3.19 are of second-order accuracy in space. Take Equation 3.17 for example. We can apply Equations 3.9 and 3.13 to it at the block-block interface $(i + 1/2, j, k)$ to get Equation 3.33, in which the remainder partial derivative terms are finite and taken around the block center (i, j, k) and at time point t_{n+1}. Then the local truncation error $\tau_{x,n+1}$ can be obtained by dividing Equation 3.17 by ρA_x and then subtracting it from Equation 3.33, resulting in Equation 3.34. Finally, we can again take the inifity norm on Equation 3.34 over the entire reservoir and at the time step t_{n+1}, and then apply the triangle inequality recursively, which will give Equation 3.35 as desired.

$$
\begin{aligned}
u_{x,i+1/2} &+ \left(\frac{k_x}{\mu}\right)_{i+1/2} \frac{p_{i+1}-p_i}{\Delta x} \\
&- \left(\frac{k_x}{\mu}\right)_{i+1/2} \frac{(\Delta x)^2}{48}\left[\left(\frac{\partial^3 p}{\partial x^3}\right)_{i+} + \left(\frac{\partial^3 p}{\partial x^3}\right)_{i-}\right] \\
&- \left(k_x\frac{\mu^*}{\mu}\right)_{i+1/2} \frac{u_{x,i+3/2}-2u_{x,i+1/2}+u_{x,i-1/2}}{(\Delta x)^2} \\
&+ \left(k_x\frac{\mu^*}{\mu}\right)_{i+1/2} \frac{(\Delta x)^2}{4!}\left[\left(\frac{\partial^4 u_x}{\partial x^4}\right)_{i+} + \left(\frac{\partial^4 u_x}{\partial x^4}\right)_{i-}\right] \\
&- \left(k_x\frac{\mu^*}{\mu}\right)_{i+1/2} \frac{u_{x,i+1/2,j+1}-2u_{x,i+1/2}+u_{x,i+1/2,j-1}}{(\Delta y)^2} \\
&+ \left(k_x\frac{\mu^*}{\mu}\right)_{i+1/2} \frac{(\Delta y)^2}{4!}\left[\left(\frac{\partial^4 u_x}{\partial y^4}\right)_{j+} + \left(\frac{\partial^4 u_x}{\partial y^4}\right)_{j-}\right] \\
&- \left(k_x\frac{\mu^*}{\mu}\right)_{i+1/2} \frac{u_{x,i+1/2,k+1}-2u_{x,i+1/2}+u_{x,i+1/2,k-1}}{(\Delta z)^2} \\
&+ \left(k_x\frac{\mu^*}{\mu}\right)_{i+1/2} \frac{(\Delta z)^2}{4!}\left[\left(\frac{\partial^4 u_x}{\partial z^4}\right)_{k+} + \left(\frac{\partial^4 u_x}{\partial z^4}\right)_{k-}\right] \\
&= 0
\end{aligned}
\tag{3.33}
$$

$$
\begin{aligned}
\tau_{x,n+1} = &- \left(\frac{k_x}{\mu}\right)_{i+1/2} \frac{(\Delta x)^2}{48}\left[\left(\frac{\partial^3 p}{\partial x^3}\right)_{i+} + \left(\frac{\partial^3 p}{\partial x^3}\right)_{i-}\right] \\
&+ \left(k_x\frac{\mu^*}{\mu}\right)_{i+1/2} \frac{(\Delta x)^2}{4!}\left[\left(\frac{\partial^4 u_x}{\partial x^4}\right)_{i+} + \left(\frac{\partial^4 u_x}{\partial x^4}\right)_{i-}\right] \\
&+ \left(k_x\frac{\mu^*}{\mu}\right)_{i+1/2} \frac{(\Delta y)^2}{4!}\left[\left(\frac{\partial^4 u_x}{\partial y^4}\right)_{j+} + \left(\frac{\partial^4 u_x}{\partial y^4}\right)_{j-}\right] \\
&+ \left(k_x\frac{\mu^*}{\mu}\right)_{i+1/2} \frac{(\Delta z)^2}{4!}\left[\left(\frac{\partial^4 u_x}{\partial z^4}\right)_{j+} + \left(\frac{\partial^4 u_x}{\partial z^4}\right)_{j-}\right]
\end{aligned}
\tag{3.34}
$$

$$\begin{aligned}\tau_{x,n+1} \leq & \left(\frac{k_x}{\mu}\right)_{i+1/2} \frac{(\Delta x)^2}{24} \left\|\frac{\partial^3 p}{\partial x^3}\right\|_\infty + \left(k_x \frac{\mu^*}{\mu}\right)_{i+1/2} \frac{(\Delta x)^2}{12} \left\|\frac{\partial^4 u_x}{\partial x^4}\right\|_\infty \\ & + \left(k_x \frac{\mu^*}{\mu}\right)_{i+1/2} \frac{(\Delta y)^2}{12} \left\|\frac{\partial^4 u_x}{\partial y^4}\right\|_\infty + \left(k_x \frac{\mu^*}{\mu}\right)_{i+1/2} \frac{(\Delta z)^2}{12} \left\|\frac{\partial^4 u_x}{\partial z^4}\right\|_\infty \\ \leq & C_x H^2 \end{aligned} \tag{3.35}$$

where

$$C_x = \left(\frac{k_x}{\mu}\right)_{i+1/2} \frac{1}{24} \left\|\frac{\partial^3 p}{\partial x^3}\right\|_\infty + \left(k_x \frac{\mu^*}{\mu}\right)_{i+1/2} \frac{1}{12} \left(\left\|\frac{\partial^4 u_x}{\partial x^4}\right\|_\infty + \left\|\frac{\partial^4 u_x}{\partial y^4}\right\|_\infty + \left\|\frac{\partial^4 u_x}{\partial z^4}\right\|_\infty \right)$$

After showing the consistency of the finite difference formulas, it is tempting to consider their stability at this stage, probably by taking advantage of the von Neuman analysis. However, proving stability is quite difficult in this case, since the fluid density ρ and viscosity μ are nonlinear functions of pressure (and temperature, which we assume constant for simplicity), so that the finite difference formulations are nonlinear as a whole. Moreover, even if we can prove stability of the finite difference formulations, it does not necessarily follow that our methods are convergent, because strictly speaking, the Lax-Richtmyer theorem is only intended for linear numerical methods approximating well-posed linear partial differential equations, not nonlinear finite difference methods or nonlinear partial differential equations. More interestingly, convergence becomes a weaker property than stability under certain circumstances, or in other words, a convergent numerical approximation method may fail to be stable [75]. Therefore, any attempt to prove stability may actually deviate from our goal of showing convergence, or even be an overkill. Nevertheless, we can relate our block-centered finite difference method on staggered grids to the lowest order Raviart-Thomas mixed finite elements [76, 77], from which its convergence property follows.

4. THE RESERVOIR SIMULATOR*

An inhouse reservoir simulator has been developed to solve the transient Stokes-Brinkman model, which draws on the framework of $FTSim$, a simulator based on the $TOUGH+$ family of codes [78]. To put things in context, we would like to first present the workflow of the simulation process, after which we will move on to the linearization and computa-tion of the finite difference model represented by Equations 3.26–3.29, and discuss some challenges that arise in the numerical simulation process.

4.1 Simulation Workflow

The simulation workflow is shown in Figure 4.1, where $\mathbf{X}$ is the vector of independent variables, including pressure p at each grid block center and velocity u at each grid block interface. At each time step, we solve for $\mathbf{X}$ iteratively by the Newton-Raphson method [74]. We begin with the solution $\mathbf{X}$ from the previous time step and use it as an initial guess for the current time step to compute the residual vector $\mathbf{R}$. Then we determine if $\mathbf{R}$ is small enough by comparing its l_2 or l_∞ norm with a preset tolerance ϵ. If so, the Newton-Raphson iteration process converges, and we accept $\mathbf{X}$ as the solution of the current time step and proceed to the next; otherwise we construct the Jacobian matrix $\mathbf{J}$, find the vector Δ by solving the linear matrix equation $\mathbf{J\Delta} = -\mathbf{R}$ with an open source incomplete LU-factorization preconditioned GMRES solver published by Ju & Burkardt [79, 80, 81], and update $\mathbf{X}$ with $\mathbf{\Delta}$. Then we go back and check the convergence again, and repeat all the steps thereafter.

By examining the workflow above, we can easily identify that the crucial step for the

*Part of this section is reprinted with permission from "Unified Finite Difference Modeling of Transient Flow in Naturally Fractured Carbonate Karst Reservoirs - A 3D Case Study" by J. He, J. E. Killough, M. M. Fadlelmula F., and M. Fraim, 2015. SPE Proceedings, Copyright [2017] by Society of Petroleum Engineers.

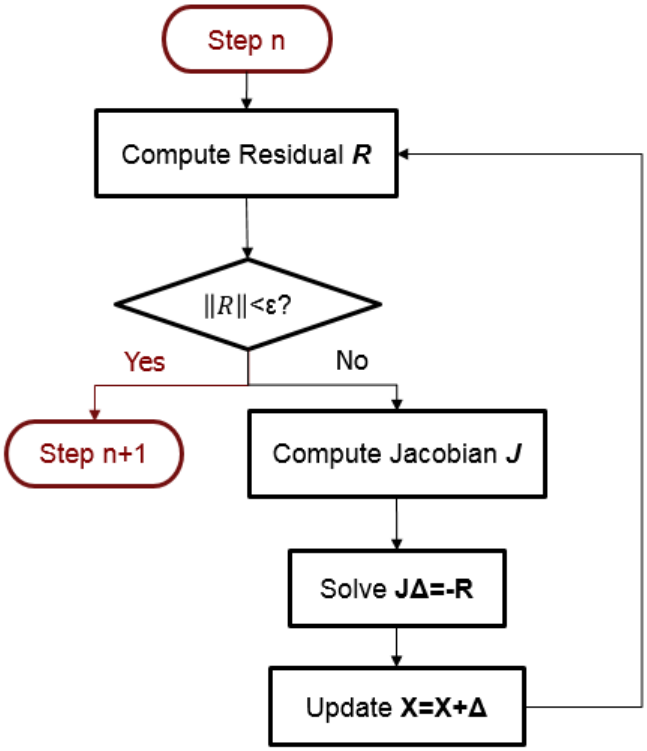

Figure 4.1: Simulation workflow for the transient Stokes-Brinkman model. [10]

Newton-Raphson iteration process is the construction of the Jacobian matrix **J**, which will be fully discussed in the next section.

4.2 Solution of the Discretized Equations

The Stokes-Brinkman equation defines a nonlinear relationship between the velocity vector u and pressure p, so that we have to solve for both of them explicitly. If we discretize the reservoir into N_x, N_y, and N_z grid blocks in the subscripted directions, and impose no-flow boundary conditions on all the six boundaries, then we will have $N_xN_yN_z$ pressure variables, $N_xN_yN_z - N_yN_z$ x-velocity variables, $N_xN_yN_z - N_xN_z$ y-velocity variables, and $N_xN_yN_z - N_xN_y$ z-velocity variables. Moreover, each pressure variable has its own

instance of Equation 3.26, and each velocity variable u_x, u_y or u_z has its own instance of the Equation 3.27, 3.28 or 3.29, respectively. In total, we have $N = 4N_xN_yN_z - N_xN_y - N_xN_z - N_yN_z$ independent variables and the same number of finite difference equations, which is necessary to achieve a unique solution.

The nonlinear system can be arranged into the following residue equation,

$$\mathbf{R}(\mathbf{X}) = \mathbf{0} \tag{4.1}$$

where $\mathbf{X}$ is the independent variable vector arranged as below,

$$\mathbf{X} = \begin{bmatrix} \mathbf{p} \\ \mathbf{u_x} \\ \mathbf{u_y} \\ \mathbf{u_z} \end{bmatrix}$$

and $\mathbf{R}$ is the residue vector of which each entry is the left-hand side of one of Equations 3.26–3.29 at whichever block center or interface the corresponding independent variable is defined. Here $\mathbf{p}$, $\mathbf{u_x}$, $\mathbf{u_y}$, $\mathbf{u_z}$ are vectors of pressure and velocities, respectively. The nonlinear system in Equation 4.1 is then linearized and iteratively solved fully implicitly at each time step $n = 0, 1, 2, \cdots$ by finding a sequence of vectors $\mathbf{X}_\upsilon^{n+1}$, $\upsilon = 1, 2, \cdots$ that converges uniformly to the true solution vector $\mathbf{X}^{n+1}$, by the Newton-Raphson method [74]:

$$\mathbf{X}_{\upsilon+1}^{n+1} = \mathbf{X}_\upsilon^{n+1} - \mathbf{J}^{-1}\left(\mathbf{X}_\upsilon^{n+1}\right)\mathbf{R}\left(\mathbf{X}_\upsilon^{n+1}\right) \tag{4.2}$$

where $\mathbf{J}^{-1}\left(\mathbf{X}_\upsilon^{n+1}\right)$ is the Jacobian matrix, and the subscript υ denotes the iteration number.

Equation 4.2 is computed iteratively until

$$\left\|\mathbf{R}\left(\mathbf{X}_{\upsilon+1}^{n+1}\right)\right\|_{\infty} < \epsilon \tag{4.3}$$

for some small tolerance ϵ, so that Equations 3.26–3.29 hold very closely at all block centers and block interfaces. In order to initialize the iterative process in Equation 4.2, we need to know $\mathbf{X}_0^{n+1}$, of which a good approximation is the convergent solution of the previous time step when $n > 0$, or the initial conditions when $n = 0$, given no drastic change in reservoir conditions between the two time steps. Besides, we have also tried quasi-Newton methods like BFGS in order to avoid computing the Jacobian matrix, but such methods turned out not to converge well for highly nonlinear systems like ours.

The full form of the Jacobian matrix $\mathbf{J}$ is

$$\mathbf{J}\left(\mathbf{X}\right) = \begin{bmatrix} \frac{\partial R_1}{\partial X_1} & \frac{\partial R_1}{\partial X_2} & \cdots & \frac{\partial R_1}{\partial X_N} \\ \frac{\partial R_2}{\partial X_1} & \frac{\partial R_2}{\partial X_2} & \cdots & \frac{\partial R_2}{\partial X_N} \\ \vdots & \vdots & \ddots & \vdots \\ \frac{\partial R_N}{\partial X_1} & \frac{\partial R_N}{\partial X_2} & \cdots & \frac{\partial R_N}{\partial X_N} \end{bmatrix} \tag{4.4}$$

where R_l and X_m, $l, m = 1, 2, \cdots, N$, are elements of the residue vector $\mathbf{R}$ and independent variable vector $\mathbf{X}$, respectively. The elements of $\mathbf{J}$ are computed numerically by forward differences, e.g.

$$\frac{\partial R_l}{\partial X_m} = \frac{R_l\left(X_m + h\right) - R_l\left(X_m\right)}{h} \tag{4.5}$$

where $h > 0$ is a small perturbation and is usually taken as 10^{-8}. We have abused the notations in Equation 4.5 since $R_l = R_l(\mathbf{X})$ is actually a function of the entire vector $\mathbf{X}$, but we have omitted the other elements of $\mathbf{X}$ for brevity and clarity, as well as to highlight

the point that only X_m is perturbed.

The numerical differentiation method represented by Equation 4.5 is preferred in the construction of the Jacobian matrix because its implementation is easier and less error prone than alternative differentiation techniques, thus allowing us to focus more on the mathematical model itself, at the cost of slightly reduced accuracy due to roundoff errors. Furthermore, it is readily observed that the Jacobian matrix for our transient Stokes-Brinkman model is sparse, multi-diagonal, nonsymmetric, and ill-conditioned, so the computation of $\mathbf{J}^{-1}\mathbf{R}$ in Equation 4.2 is difficult and time consuming. In our simulator, a restarted generalized minimal residual (GMRES) solver [79, 80] is employed to address this issue, which builds on the compressed row storage format and is armed with an incomplete LU factorization preconditioner.

4.3 The Newton-Raphson Method

The Newton-Raphson method is named after Isaac Newton and Joseph Raphson who developed the first versions of this method in the late 17th century. In this section, we derive the Newton-Raphson method from the n-dimensional second-order Taylor series approximation for a smooth function $f(\mathbf{x})$ [74]:

$$f(\mathbf{x}+\mathbf{p}) \approx f(\mathbf{x}) + \mathbf{p}^T \bigtriangledown f(\mathbf{x}) + \frac{1}{2}\mathbf{p}^T \bigtriangledown^2 f(\mathbf{x})\,\mathbf{p} \tag{4.6}$$

where $\mathbf{x}$ is a vector of n independent variables. Essentially, Equation 4.6 approximates the value of the smooth function f at any point $\mathbf{x}+\mathbf{p}$ around the fixed point $\mathbf{x}$ with a quadratic function of the distance vector $\mathbf{p}$, at the cost of a third-order truncation error.

The derivative of Equation 4.6 against $\mathbf{p}$ is

$$f'(\mathbf{x}+\mathbf{p}) = \bigtriangledown f(\mathbf{x}) + \bigtriangledown^2 f(\mathbf{x})\,\mathbf{p} \tag{4.7}$$

By simply setting $f^{'}(\mathbf{x}+\mathbf{p}) = \mathbf{0}$ in the Equation 4.7, we obtain the following explicit formula:

$$\mathbf{p}^{*} = -\left(\bigtriangledown^{2} f(\mathbf{x})\right)^{-1} \bigtriangledown f(\mathbf{x}) \tag{4.8}$$

If the Hessian matrix $\bigtriangledown^{2} f(\mathbf{x})$ is positive-definite, then Equation 4.7 attains its minimum at the point $\mathbf{x}+\mathbf{p}^{*}$. Moreover, since Equation 4.7 closely approximates the function $f(\mathbf{x})$ in the neighborhood of $\mathbf{x}$, it is reasonable to anticipate that the point $\mathbf{x}+\mathbf{p}^{*}$ should be at least close enough to, if not exactly, the local minimizer of the function $f(\mathbf{x})$. Combining these insights would allow us to iteratively construct a sequence of points $\mathbf{x}_0, \mathbf{x}_1, \cdots, \mathbf{x}_n, \cdots$ from an initial point $\mathbf{x}_0$, i.e. an appropriate initial guess of the true solution of the function $f(\mathbf{x})$, such that

$$\mathbf{x}_{n+1} = \mathbf{x}_n + \mathbf{p}_n^{*} = \mathbf{x}_n - \left(\bigtriangledown^{2} f(\mathbf{x}_n)\right)^{-1} \bigtriangledown f(\mathbf{x}_n) \tag{4.9}$$

Equation 4.9 represents the modern Newton-Raphson method, which effectively minimizes the value of the target function $f(\mathbf{x})$ by descending from one point to another in the direction of a most probable local minimizer, and is widely applied in the numerical solution of nonlinear continuous optimization problems. In addition, because of the equivalence relationship between minimization of Equation 4.6 and solution of Equation 4.7, the Newton-Raphson method also applies to the solution of discrete nonlinear systems, which can be thought of as the gradients of some multivariate functions.

5. SIMULATION RESULTS*

In this chapter, I would like to illustrate the transient Stokes-Brinkman model with several 2D and 3D reservoir simulation case studies. The simulation inputs, i.e. the fluid properties and some universal reservoir properties are presented in the first section, which is followed by various reservoir models and their simulation results.

5.1 Fluid Properties

Liquid n-octane is chosen as the single-phase oil in our simulation. The density ρ and viscosity μ of liquid n-octane are calculated as functions of pressure p and temperature T through the following Yaws' models [12]:

$$\rho = a \cdot b^{-(1-T/T_c)^d} \cdot e^{c_o\left(p-p_{ref}\right)} \tag{5.1}$$

$$\log_{10}\mu = B + \frac{C}{T} + DT + ET^2 \tag{5.2}$$

where p_{ref} is the reference pressure, T_c is the critical temperature, a, b, d, B, C, D and E are coefficients that pertain to the specific liquid, and c_o is the oil compressibility. Equation 5.1 is plotted in Figure 5.1 for typical reservoir temperatures and pressures, and Equation 5.2 in Figure 5.2 against its applicable temperature range. It is also worth noting that the original Yaws' liquid density model ignores the effect of pressure change on liquid density,

*Part of this section is reprinted with permission from "A Unified Finite Difference Model for The Simulation of Transient Flow in Naturally Fractured Carbonate Karst Reservoirs" by J. He, J. E. Killough, M. M. Fadlelmula F., and M. Fraim, 2015. SPE Proceedings, Copyright [2017] by Society of Petroleum Engineers, and "Unified Finite Difference Modeling of Transient Flow in Naturally Fractured Carbonate Karst Reservoirs - A 3D Case Study" by J. He, J. E. Killough, M. M. Fadlelmula F., and M. Fraim, 2015. SPE Proceedings, Copyright [2017] by Society of Petroleum Engineers, and "Discrete Fracture-Vug Network Modeling in Naturally Fractured Vuggy Reservoirs Using Multiple-Point Geostatistics: A Micro-Scale Case" by M. M. Fadlelmula F., M. Fraim, J. He, and J. E. Killough, 2015. SPE Proceedings, Copyright [2017] by Society of Petroleum Engineers.

which is remedied in Equation 5.1 by multiplying the right-hand side of the equation with $e^{c_o(p-p_{ref})}$. In other words, we have assumed constant oil compressibility in the pressure range of our simulation and that the original Yaws' model gives liquid densities at the reference pressure. These assumptions are by no means realistic, but are deemed good approximations for our study of incompressible and slightly compressible fluids.

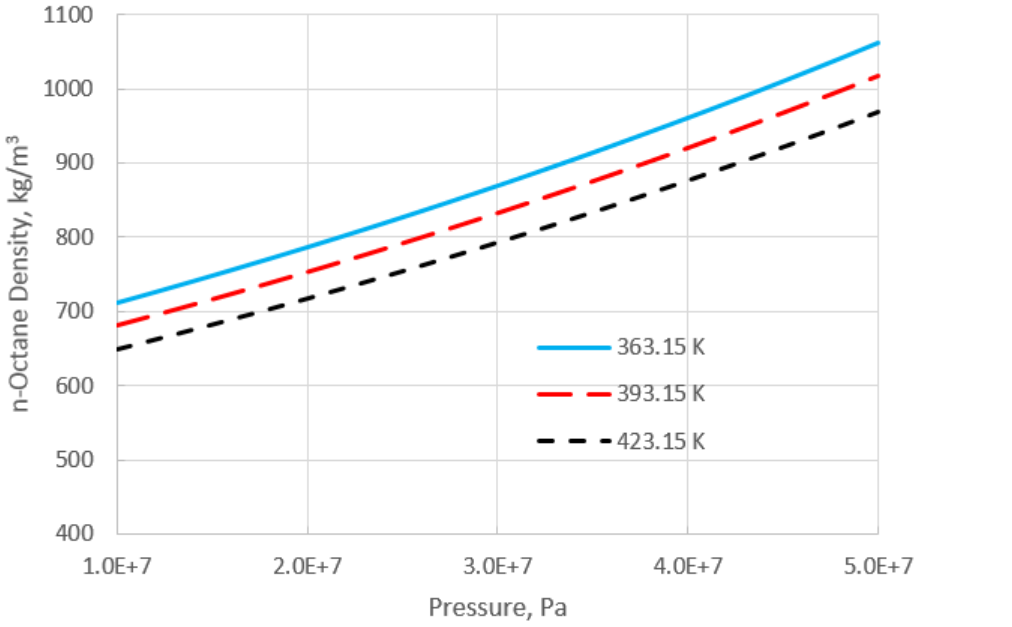

Figure 5.1: Yaws' density model for n-octane.

The values of the fluid property coefficients, along with other reservoir properties and computational parameters, are listed in Tables 5.1 and 5.2. In particular, we only consider homogeneous porous media in our examples, and use a default permeability ratio $k_f/k_m = 1000$, where k_f denotes the karst/fracture permeability and k_m the permeability of porous media. Two wells are placed in the reservoirs to form the classic quarter five-spot pattern, of which the well locations and mass flow rates are given in Table 5.3. Unless otherwise stated, these two tables are used as the standard inputs for all the following case studies, so as to single out the effect of different reservoir structures.

5.2 2D Case Studies

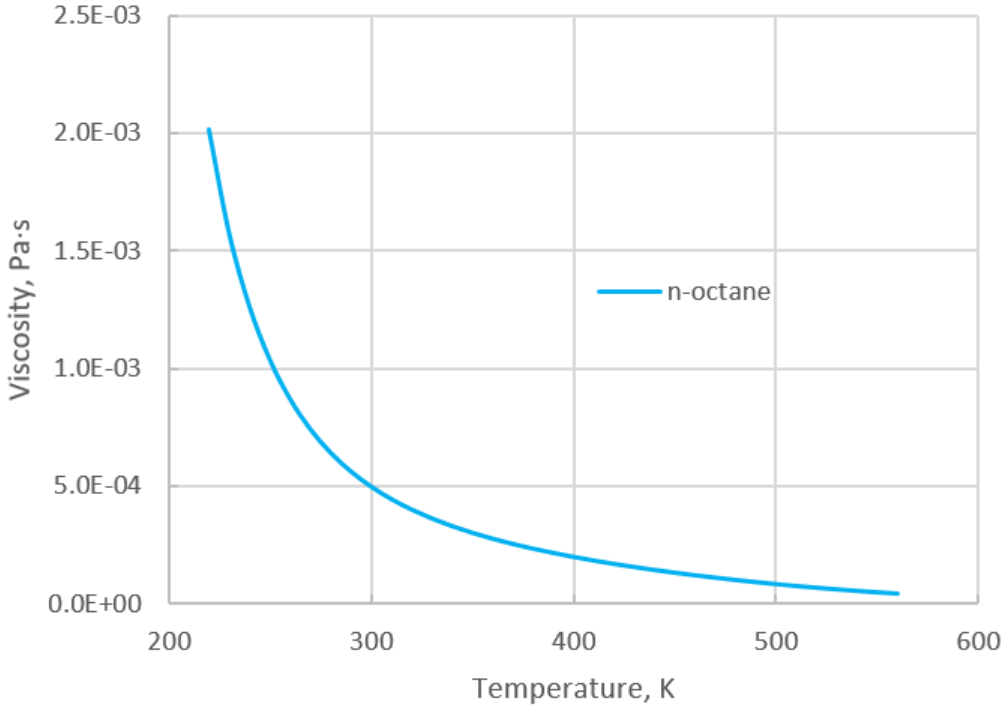

Figure 5.2: Yaws' viscosity model for n-octane.

Property	**Value**	**Units**
Oil Density Coefficients		
a	0.22807	$kg/m3$
b	0.25476	$-$
T_c	568.83	K
d	0.26940	$-$
c_o	1.0×10^{-8}	Pa^{-1}
p_{ref}	1.0×10^{5}	Pa
Oil Viscosity Coefficients		
B	-8.9245	$-$
C	888.09	K
D	0.012955	K^{-1}
E	-1.3596×10^{-5}	K^{-2}

Table 5.1: Fluid properties [12].

Property	**Value**	**Units**
Porous Medium Properties		
k_m	1.5×10^{-14}	m^2
ϕ_m	0.15	$-$
Karst and Fracture Properties		
k_f/k_m	10^3	$-$
ϕ_f	1.0	$-$
Grid Parameters		
N_x	100	$-$
N_y	100	$-$
N_z	1	$-$
Δx	20	m
Δy	20	m
Δz	20	m
Initial Conditions		
p_{ic}	3.0×10^7	Pa
T_{ic}	90	$^\circ C$
Computational Parameters		
ϵ	1.0×10^{-6}	$-$
h	1.0×10^{-8}	$-$

Table 5.2: Reservoir properties and computational parameters [13].

Well Number	**Location** (i, j, k)	**Rate** (kg/s)
1	$(1, 1, 1)$	-3.0
2	$(100, 100, 1)$	3.0

Table 5.3: Well properties [13].

The transient Stokes-Brinkman model is illustrated with the simulation results of three 2D reservoir models. The first 2D model merely comprises homogeneous porous media, and is used to test our simulator in the Darcy flow region. The second 2D model is borrowed from Gulbransen et al. [50], which is synthesized to contain karst connected by natural fractures. The third model is derived with the multiple-point geostatistical (MPG) simulation technique by using the second model as the training image. The geological

structures of the last two models are presented in Figure 5.3, and the standard fluid and reservoir properties listed in Tables 5.1–5.3 are applied to all three models unless otherwise specified.

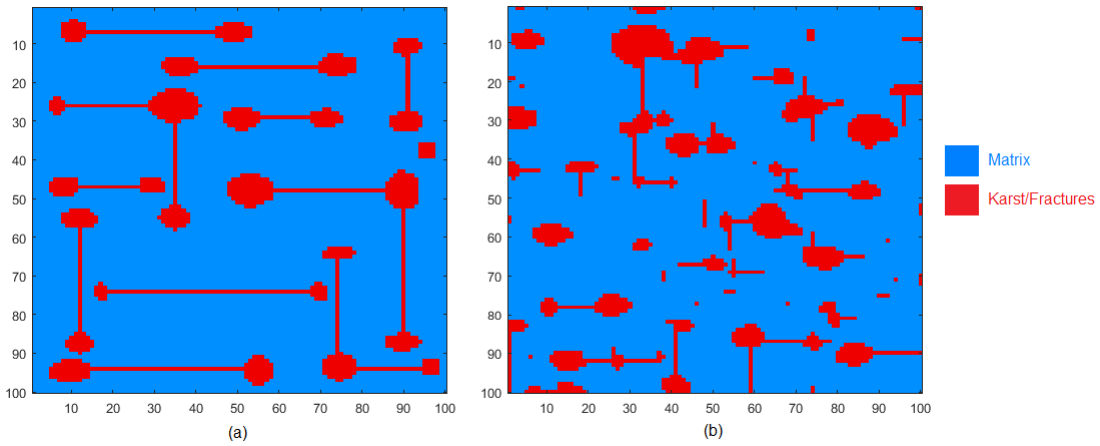

Figure 5.3: Geological structures of the (a) synthetic and (b) derived reservoir models.

5.2.1 Pure Porous Media

We first test our Stokes-Brinkman simulator in pure homogeneous porous media with properties specified in Tables 5.2 and 5.3. The simulation results at 100 days are visualized in Figure 5.4, with the pressure field in the form of natural logarithmic pressure distribution, and the velocity field in the form of streamlines [82]. Both plots exhibit clear radial flow patterns symmetric with respect to the injection well in the upper left corner and the production well in the lower right corner, demonstrating that our simulator works well in the Darcy flow region.

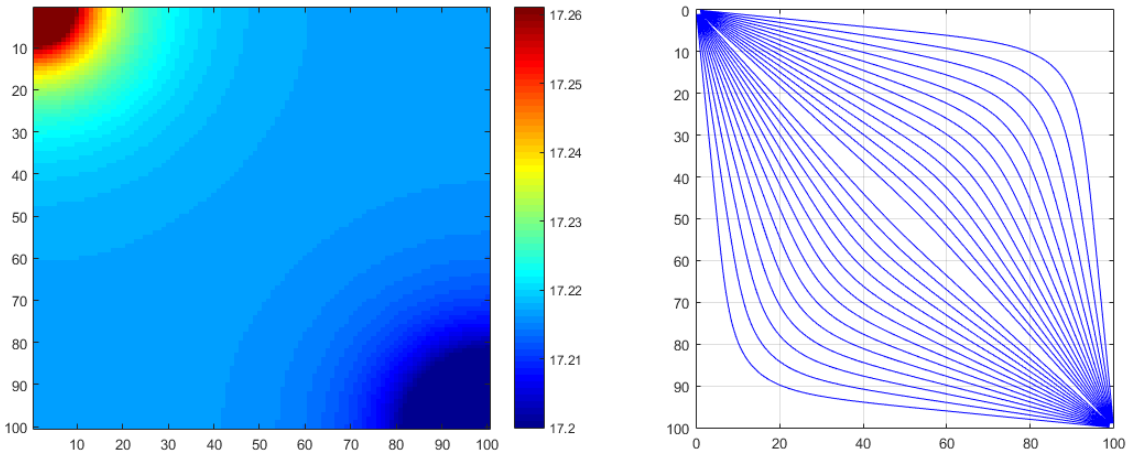

Figure 5.4: Simulation results at 100 days, pure porous media.

5.2.2 Synthetic Reservoir Model

A 2D synthetic reservoir model is binarized from the one studied by Gulbransen et al. [50] using $TiConverter$ [83], a self-developed Visual Basic code. The pressure and velocity fields for this synthetic model are displayed in Figure 5.5, again in the forms of logarithmic pressure distributions and streamlines. Figure 5.5c illustrates that the presence of karst and fractures (as labeled in red in Figure 5.3) significantly distorts the isobars and streamlines from the radial flow pattern depicted in Figure 5.4. The streamline plots on the right side of Figure 5.5 also demonstrates how the majority of fluid flow in the synthetic reservoir is converged by and channeled through the natural fractures, while the dynamic reachout of the pressure front could be observed from the left side of Figure 5.5, which is dictated by the fracture orientation so that whenever the pressure front reaches one of two interconnected karsts, it quickly spreads over through the fracture to the other karst, much faster than it propagates from the karsts and fractures into the porous media. Moreover, if we set $\mu^* = 0$ throughout the reservoir, then the Stokes-Brinkman model degenerates to the conventional Darcy flow model, of which the simulation results, as shown in Figure

5.6, are only slightly different from those of the Stokes-Brinkman model. A histogram is further constrctucted in Figure 5.7 for the pressure differences between the two models at all the grid block centers in 100 days, showing that the pressure differences range from zero to a maximum of approximately $8 \times 10^4 Pa$, depending on the distance of the grid blocks to the wells.

5.2.3 Derived Reservoir Model

The synthetic reservoir model in Figure 5.3a is treated as a training image to generate a 2D reservoir model with the MPG simulation technique. For this purpose the Single Normal Equation Simulation (SNESIM) algorithm of Stanford Geostatistical Modeling Software is used [84], and the generated model is conditioned to the facies data (binary indicators for matrix and karsts having proportions of 0.546 and 0.454, respectively) of Stanford VI dataset [85]. The conditioned reservoir model is shown in Figure 5.3b as our derived model, and the SNESIM parameters used to generate this 2D model are listed in Table 5.4. Compared with the synthetic model, most of the karsts in the derived model are isolated and few are interconnected by fractures. Accordingly, the pressure and velocity fields in Figure 5.8 are less distorted from radial flow than those in Figure 5.5, suggesting that the presence of karst alone does not substantially alter the flow patterns in the reservoir. The simulation results of the Darcy flow model are displayed in Figure 5.9 as well, which, similar to the previous example, are only slightly different from those of the Stokes-Brinkman model. Further examination of the histogram in Figure 5.10 convinces us that the pressure differences between the two models are from zero to a maximum of approximately $10^5 Pa$, again depending on the distance of the grid blocks to the wells.

To summarize, among the above three fine-scale 2D reservoir models, the first model demonstrates that the Stokes-Brinkman model can reduce to Darcy flow correctly, which

forms the basis on which the correctness of the general model has to be built. It's been controversial for a long time in the oil and gas research community whether fluid flow in connected vugs is different from that in isolated vugs. The second and third models represent these two scenarios, and their simluation results reveal that the presence of karsts interconnected by natural fractures significantly alters the pattern of fluid transport in the naturally fractured carbonate karst reservoir, while karsts alone have similar but much weaker effects. Further comparison with the Darcy flow model shows that the Stokes-Brinkman model indeed yields different simulation results, though the differences are only significant around the wells. These results form the foundation for further investigation of 3D and multiphase cases.

Parameter	**Value**
Seed	211175
# of Categories	2
Target Marginal Distribution	0.546, 0.454
# of Nodes in Search Template	60
Search Template Geometry (ranges and angles)	21, 21, 21 and 0, 0, 0
Hard Data (property)	Facies
Min # of Replicates	1
Servosystem Factor	0
Re-simulation Threshold	-1
Re-simulation Iteration #	1
# of Multigrids	3
Previously Simulated Nodes	4
Template Expansion	Isotropic
Training image	Figure 5.3a

Table 5.4: SNESIM parameters [13].

5.3 3D Case Study

The 3D naturally fractured vuggy reservoir model, as shown in Figures 5.11–5.13, is derived from a carbonate core that is $2.0in$ in height and $1.45in$ in diameter sampled from the Shuaiba Formation in the Arabian Gulf area. A cubic plug with a face area of $5mm^2$ is cut from the core sample, and scanned with a CT scanner to get images of slices having a size of 960×1005 pixels. The images are cropped and segmented using Avizo software, and the small micro-factures in the original images are lost during the segmentation process as a result of smoothing and denoising. Three of these images are used as matrix-vug images for our 3D reservoir model. Additionally, we get three fracture network images by drawing fractures of constant width in their present locations in each of the three layers. In total, six images are obtained, all of which are resized to 100×100 pixels using TiConverter, an inhouse software which helps retain the geological structures when shrinking the images. Finally, The six images are combined into three fracture-vug-matrix images (i.e. the three layers of the reservoir model) by superimposing the fracture network images on their corresponding matrix-vug images [11, 86].

For the flow simulation study, an injection well is placed in Block $(10,\ 10,\ 1\ )$, and a production well in $Block(91, 91, 1)$ of the reservoir model. The injection well is at a constant rate, and the production well is described by the following simple equation

$$m = WI\,(p - p_{bh}) \tag{5.3}$$

where m is the mass production rate, p the pressure of the grid block, WI the production well index, and p_{bh} the constant bottomhole pressure of the well. We assume a constant

well index for Equation 5.3 in our simulation case study, while more complicated well index models can be found in [87, 37, 88].

The reservoir properties and computational parameters are as in Table 5.2, except that each layer of the reservoir only has 100×100 grid blocks. The well parameters are displayed in Table 5.5. In particular, the microscale model obtained from the core plug is enlarged so that vugs and fractures actually become caves and valleys, which serves solely as an increase in orders of magnitude for the simulation results. Moreover, we assume the reservoir to be homogeneous and isotropic for simplicity. The porosity of fractures and vugs is unchangeably 1.0, and by default the vug-fracture permeability is set to 1000 times of the matrix permeability. The single-phase fluid is again liquid n-octane, of which the density and viscosity are calculated from Equations 5.1 and 5.2.

Property	**Value**	**Units**
Injection Rate	3.0	$kg \cdot s^{-1}$
Bottomhole pressure	1.0×10^7	Pa
Well index	3.0×10^7	$kg \cdot s^{-1} \cdot Pa^{-1}$

Table 5.5: Well parameters for the 3D model [10].

The pressure distribution at 100 days is displayed in Figure 5.14 for each of the three reservoir layers, respectively. In order to get the best contrast, we have indeed plotted the logarithm of pressure and adjusted the color scale for each graph. By comparing with Figures 5.11–5.13, it is evident that the pressure contours in every layer honor the presence of vugs and fractures in that layer, which is consistent with our observations in the 2D case studies. Furthermore, a closer examination of the two figures reveals that the pressure contours are also affected by the geological structures in adjacent layers. For example, the bright areas to the right of the middle of Figures 5.14a–5.14c correspond to

the compacted fractures at the same location in Figure 5.11, while the shape of these bright areas in Figures 5.12 and 5.13 are also slightly distorted through their connection to vugs and fractures right below.

The volumetric flow rate of the production well is plotted over time in Figure 5.15 for different k_f/k_m ratios, where k_f is the permeability of fractures and vugs, and k_m is the permeability of the porous medium. The volumetric flow rate is converted from mass flow rate of n-octane at stock-tank conditions, namely, $101325Pa$ and $16°C$. It is not surprising that the flow rate curve rises as the permeability ratio k_f/k_m increases. However, the predicted 100-day flow rate of a permeability ratio of 2000 is merely less than 2% more than that of 50, and the differences between predicted 100-day flow rates of permeability ratios of 100–2000 are within 1%, which is perfect considering the uncertainties of the input data in real practices, and suggests that any attempts to accurately estimate fracture/vug permeability or to use a permeability ratio greater than 2000 times are redundant for flow simulation purposes since little improvement can be achieved in flow rate prediction through such attempts. Moreover, Figure 5.16 shows that the computational time of the transient Brinkman model grows as the permeability ratio k_f/k_m increases, since the Jacobian matrix gets more ill-conditioned and thus leads to less stable solutions and more Newton iterations, while much greater k_f/k_m values, e.g. 10^6, will run the simulator forever or even crash it. Therefore, the k_f/k_m ratio should also be limited to a maximum of 2000 from the aspect of maintaining numerical stability of the simulation process. The above discussions justify our default choice of a permeability ratio of 1000 which minimizes numerical errors with moderate computational cost.

If we take $\mu^* = 0$ in the entire carbonate reservoir, i.e. we assume Darcy flow only and run the simulation with the same model inputs, then we will get production curves that almost overlap those in Figure 5.15, which indicates that, as expected, the nonlinear term $\mu^*\Delta\mathbf{u}$ in the Stokes-Brinkman equation is almost negligible. In other words, Darcy's law

describes fluid flow in fractures and karst properly only if we view it as a mathematical simplification of the Stokes-Brinkman equation. These findings have further implications since as far as the Stokes-Brinkman equation is concerned, the permeability tensor $\mathbf{k}$ in the fractured and karst regions has no physical meanings. $\mathbf{k}$ is a pure mathematical coefficient in those regions which we should let go to infinity, and as shown above, by infinity we mean a k_f/k_m ratio of 1000 or so. This conclusion is contradictory to the popular belief that isolated vugs should have much lower permeability values than the connected ones.

5.4 Application to Carbonate Reservoir Characterization

As can be seen from the previous sections, geological models are the indispensable input data for the reservoir simulation process. Conversely, we can also use our reservoir simulator to evaluate how closely the geological models represent the real reservoir in turns of connectivity and flow performance. Here we take the example of the carbonate core that is $2.0in$ in height and $1.45in$ in diameter sampled from the Shuaiba Formation in the Arabian Gulf area, of which the CT scanning images were used to generate the 3D naturally fractured vuggy reservoir model in Figures 5.11–5.13. To have three different structures in our geological model, the fractures are assumed to have a constant width, and then they are drawn manually in their locations in the original model. The drawn fracture network is superimposed on the segmented image to generate the three-structure micro-scale geological model having a size of $192 \times 192 \times 1$ pixels. Figure 5.17 shows how this model is generated.

The final geological model shown in Figure 5.17d is considered as the reference model in the present study, and used to generate the MPG realizations in Figure 5.18. We then

followed two different approaches in MPG to generate 30 equiprobable models (or realizations) that mimic the discrete fracture-vug networks (DFVN) of Figure 5.18b, respectively. The first one directly uses the reference model in Figure 5.18 as the training image and is thus called the "direct method" while the second uses the training images of Figure 5.19 and is called the "combination method", since the structures in the reference model are separated into matrix-fracture and matrix-vug to generate the two new models in Figure 5.19. The generated realizations of both methods honored the hard data. In Figure 5.20, the reference model and three realizations from each method are shown. Clearly, the three structures of the reference model are reproduced in the realizations of both methods. However, by comparing the proportions of the structures in these realization it is obvious that the combined method yields better results than the direct method. To clarify, the matrix and fracture proportion in the realization of the direct method are underestimated while only the fracture is underestimated in the combination method. The fracture underestimation in the combination method is due to the correction of intersection cases (see Figure 5.21). Therefore, the use of secondary data to constrain the combination MPG modeling method proposed in this study is expected to improve the results significantly. In addition, from a visual perspective, Figure 5.20 shows that the reproduction of vugs patterns is better than that of the fractures in both methods. Nevertheless, the models of both methods succeeded in reproducing the spatial continuity of the refrence model, as can be seen from the variograms in Figures 5.22 and 5.23.

To further support the findings that the combination method yields better spatial connectivity than the direct method, we would like to further investigate the flow performances of the models generated by both methods and compare them with that of the reference model, by running them with the reservoir simulator we have developed based on the transient Stoke-Brinkman model. The same fluid and reservoir properties are used as presented in Equations 5.1 and 5.2, and Tables 5.1 and 5.2, except that the grid block size is

$10m \times 10m \times 10m$. An injector is put in Block $(2, 2)$, and a producer in Block $(191, 191)$, with well properties described in Table 5.3.

The production rates of 30 direct models and 30 combination models are plotted against time in Figures 5.24 and 5.25, respectively. The production rates are volumetric and converted from mass flow rates at stock tank conditions, namely $101325Pa$ and $16°C$. The flow rate curves of the direct models are grouped into two types, and those of the combination ones into four types. By comparing the two graphs, it is easy to see that the Type 2 curves of the combination models diverge from the reference model at a much later time, and that both Type 2 and Type 3 curves of the combination models are much closer to the reference model than the other curves. The results show that the combination method surpasses the direct one in the sense that the former has a higher chance of generating realizations that better represent the real geological model. It is also worth noting that even the best case in Figure 5.25 still has a considerable deviation from the reference model at the end of the simulation, due to the effect of fracture underestimation as mentioned earlier. Moreover, these results encourage the use of MPG in modeling DFVN for field-scale cases. In such cases, the geological DFVN models (i.e. training images) can be generated using the statistical information of fractures and vugs, as in the case of discrete fracture network modeling, and outcrop images.

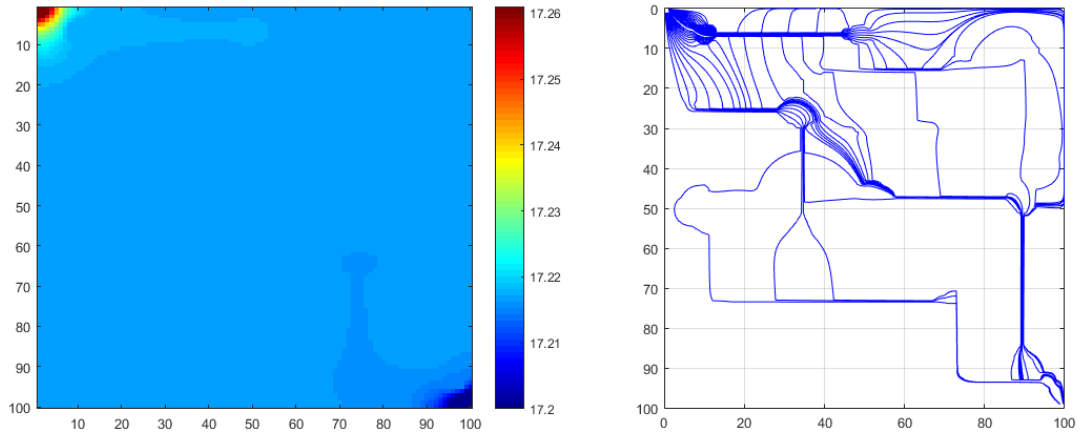

(a) 10 days

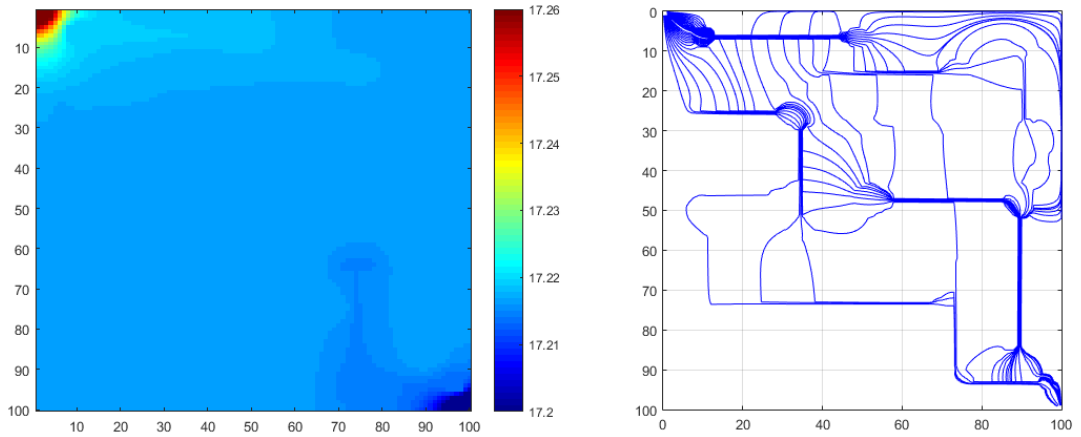

(b) 50 days

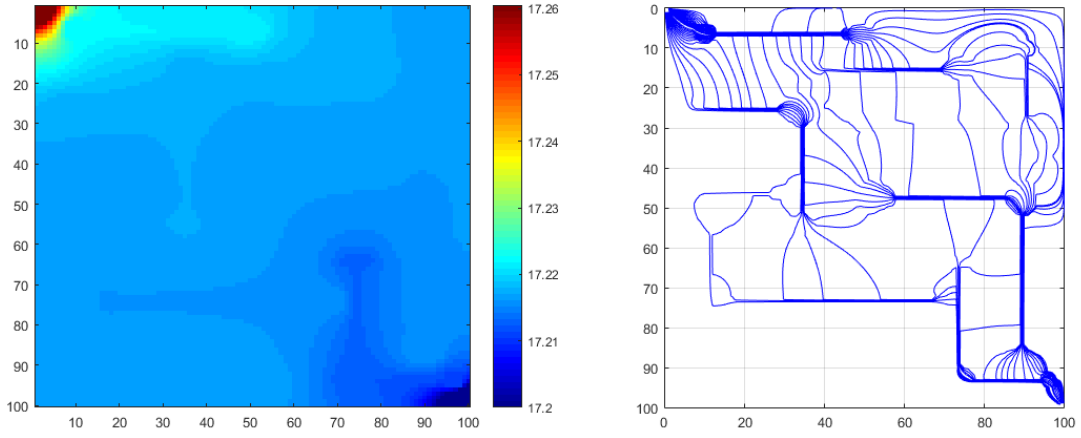

(c) 100 days

Figure 5.5: Pressure distributions (left) and streamlines (right) at different time points, synthetic reservoir, Stokes-Brinkman model.

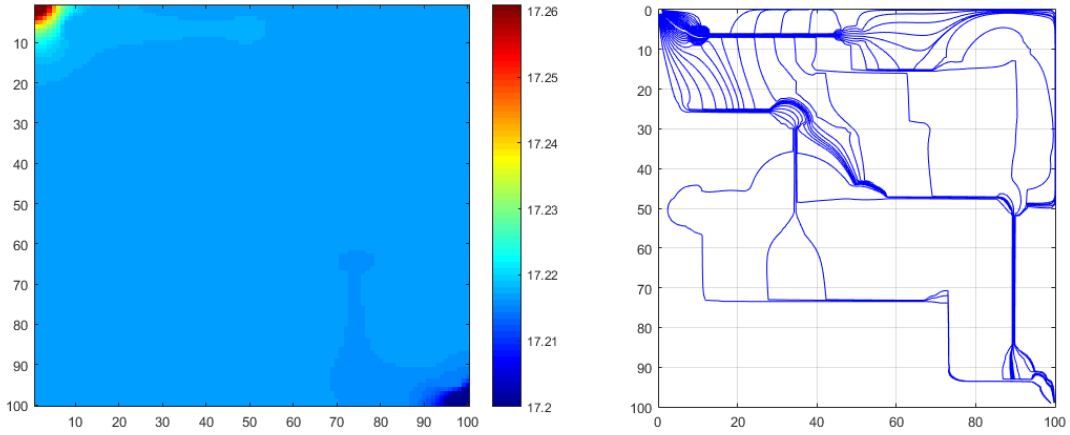

(a) 10 days

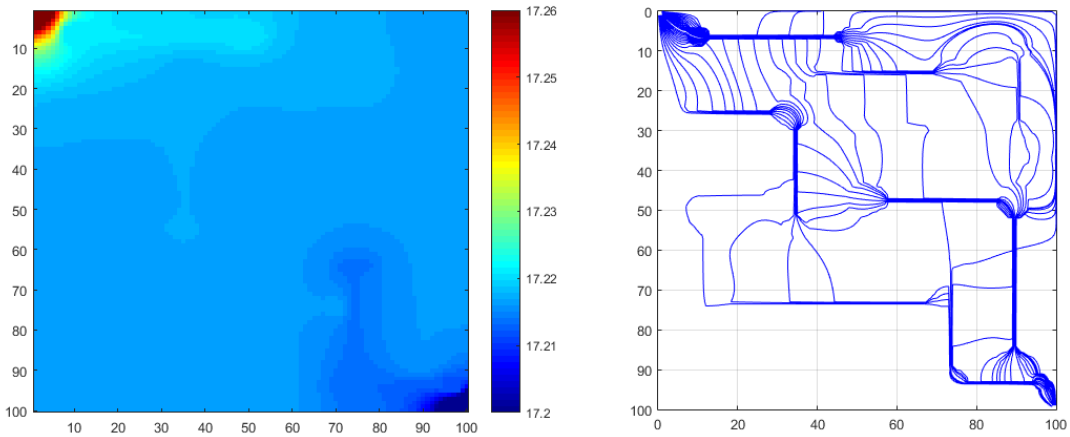

(b) 50 days

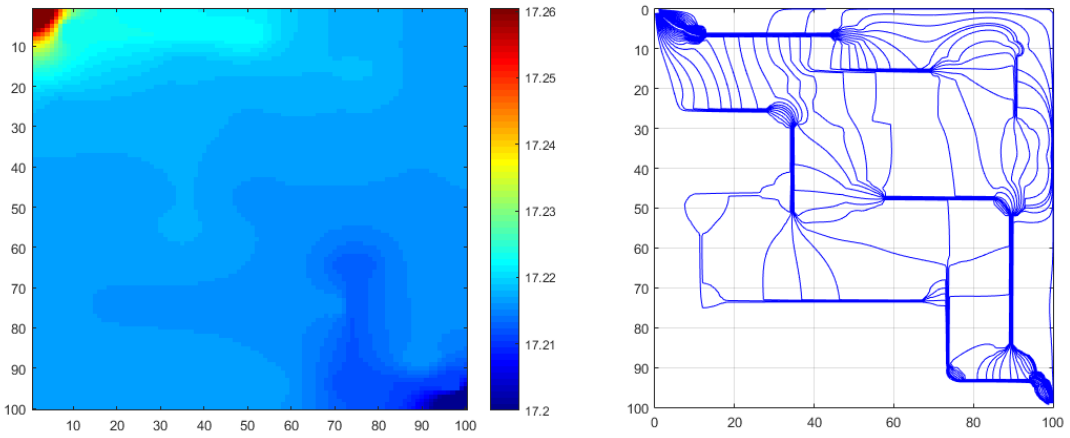

(c) 100 days

Figure 5.6: Pressure distributions (left) and streamlines (right) at different time points, synthetic reservoir, Darcy flow model.

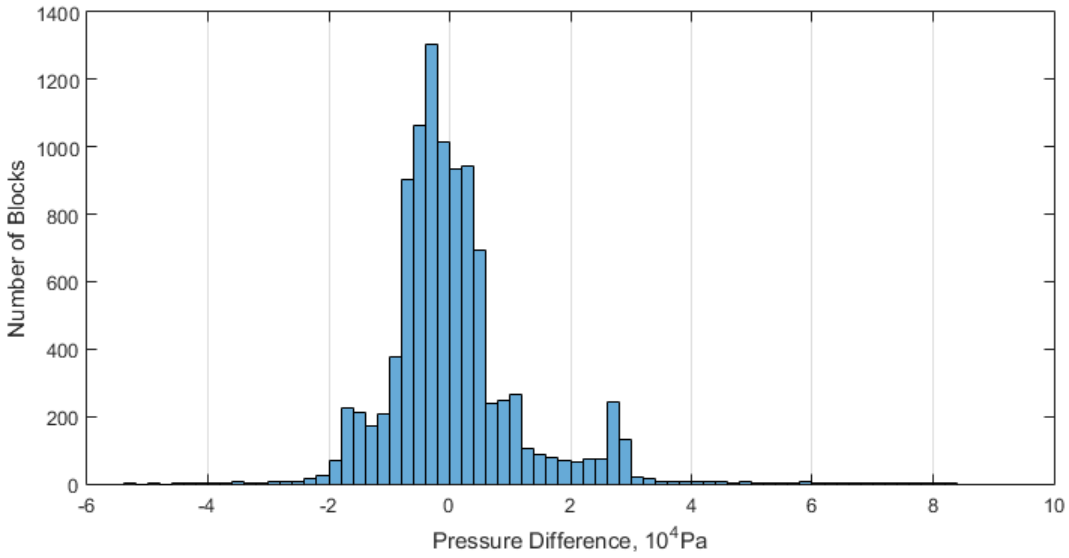

Figure 5.7: Histogram for the pressure differences, synthetic model.

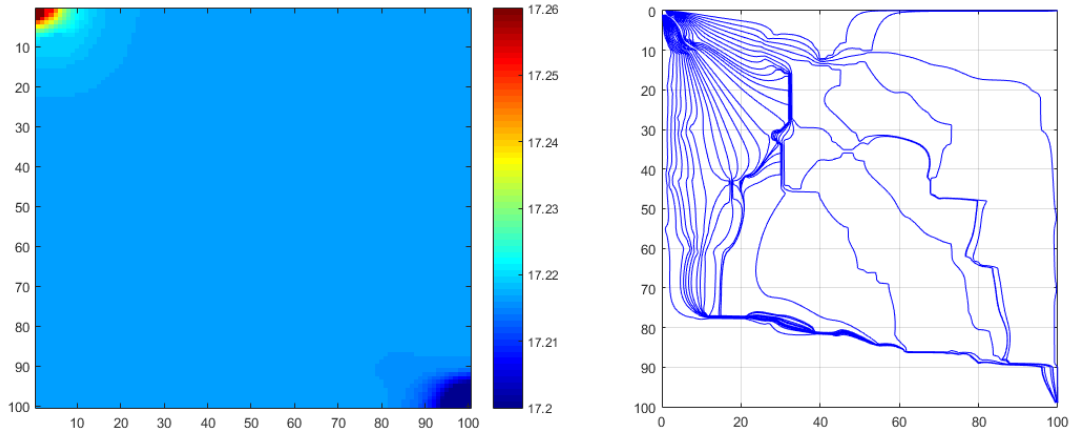

(a) 10 days

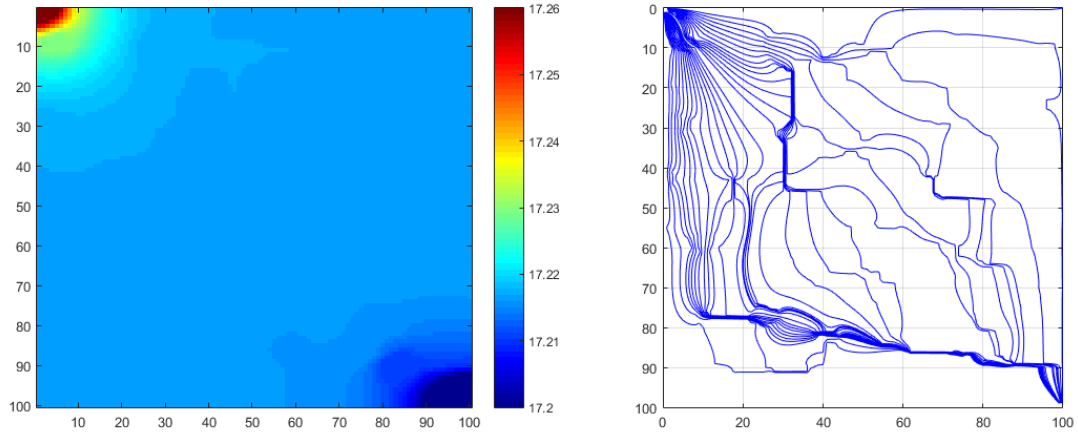

(b) 50 days

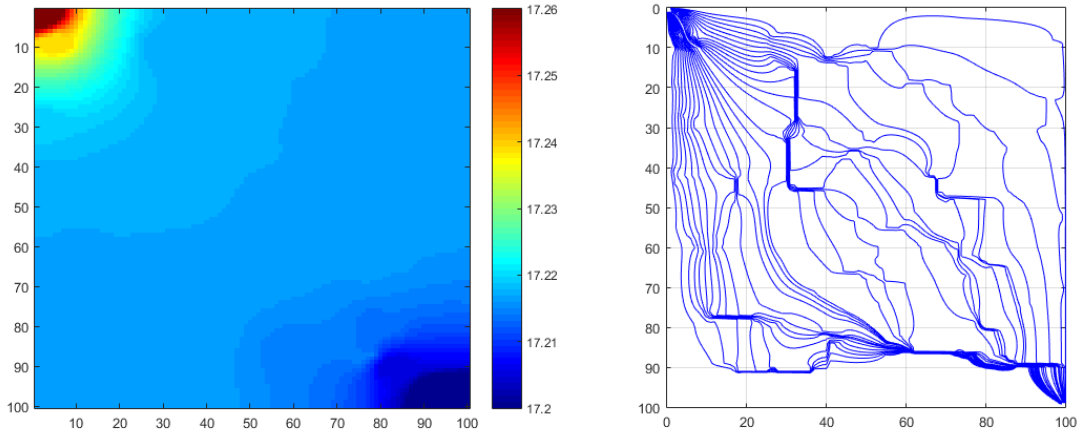

(c) 100 days

Figure 5.8: Pressure distributions (left) and streamlines (right) at different time points, derived reservoir, Stokes-Brinkman model.

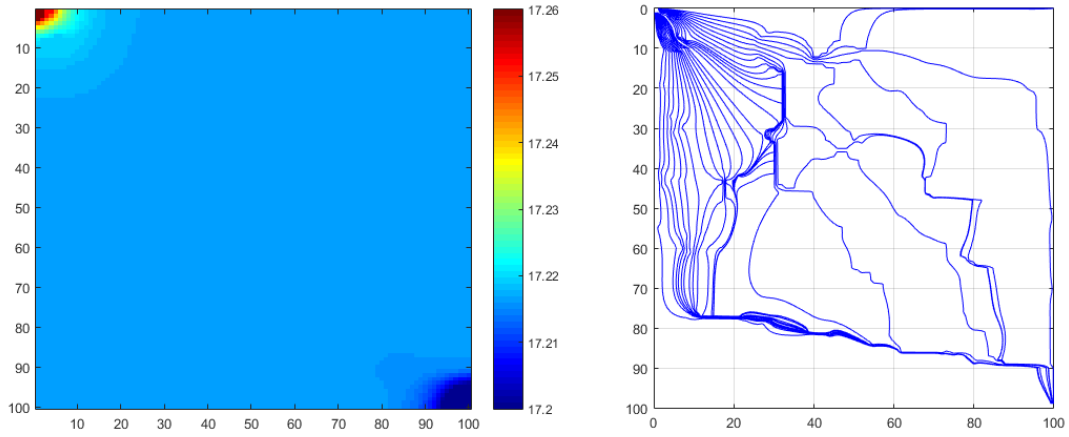

(a) 10 days

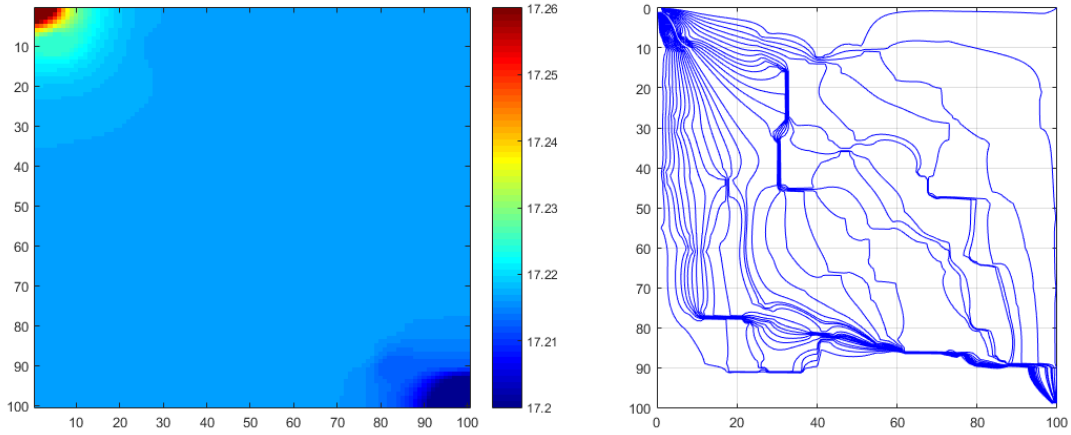

(b) 50 days

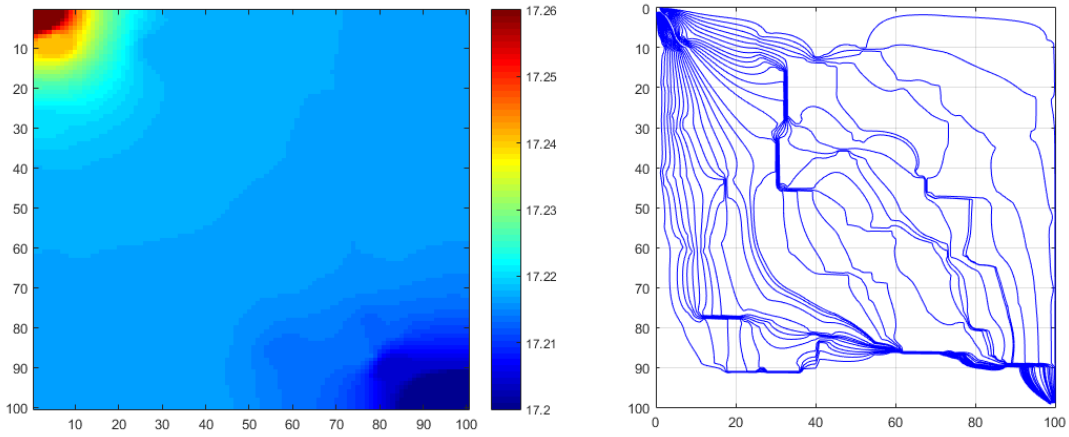

(c) 100 days

Figure 5.9: Pressure distributions (left) and streamlines (right) at different time points, derived reservoir, Darcy flow model.

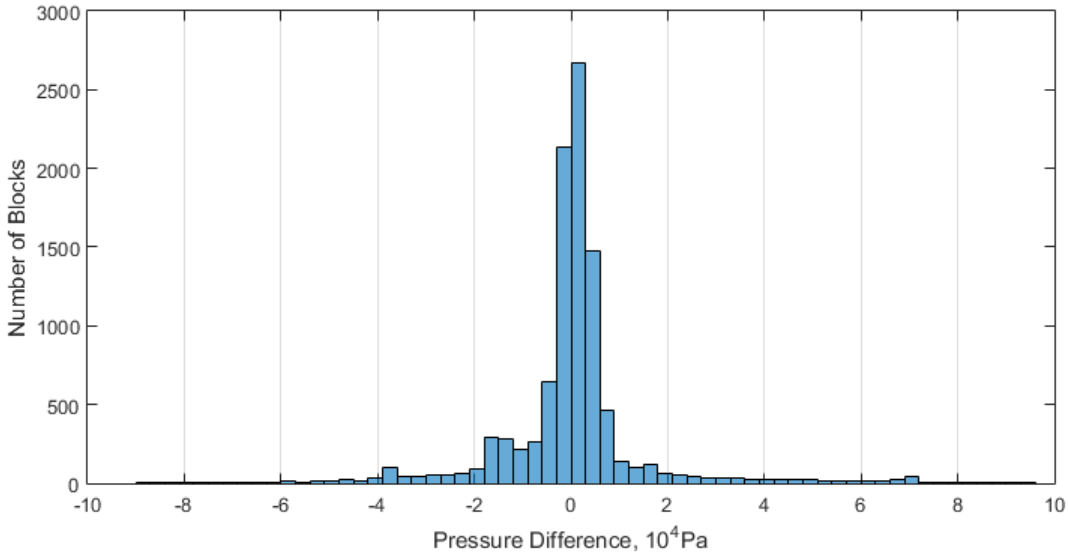

Figure 5.10: Histogram for the pressure differences, derived model.

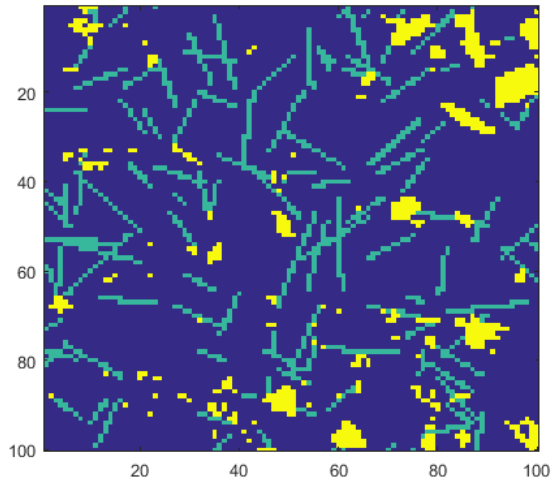

Figure 5.11: Geological structure of the $100 \times 100 \times 3$ naturally fractured carbonate karst reservoir, top layer [10].

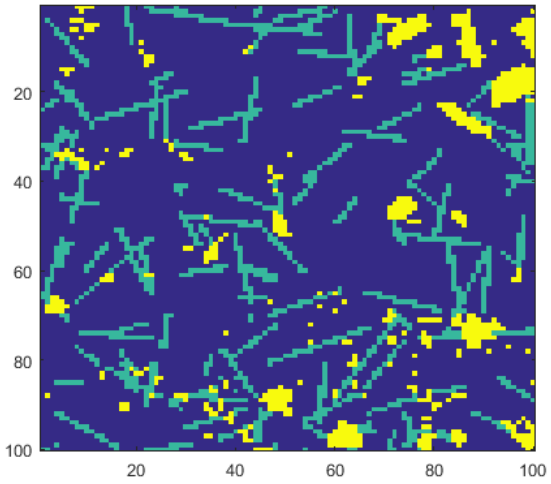

Figure 5.12: Geological structure of the $100 \times 100 \times 3$ naturally fractured carbonate karst reservoir, middle layer [10].

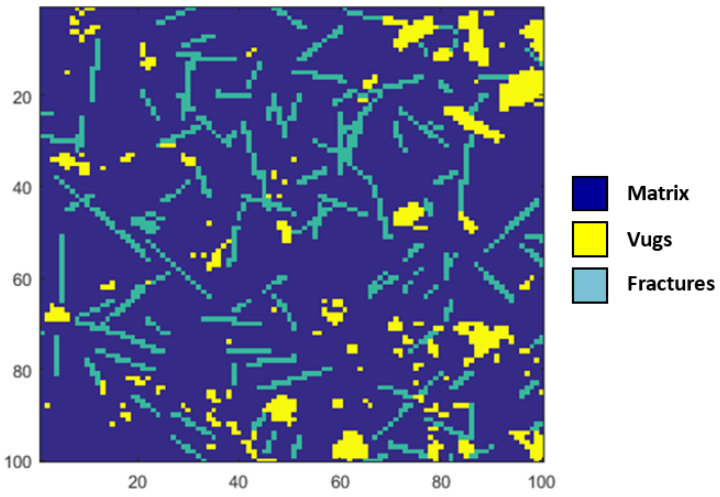

Figure 5.13: Geological structure of the $100 \times 100 \times 3$ naturally fractured carbonate karst reservoir, bottom layer [10].

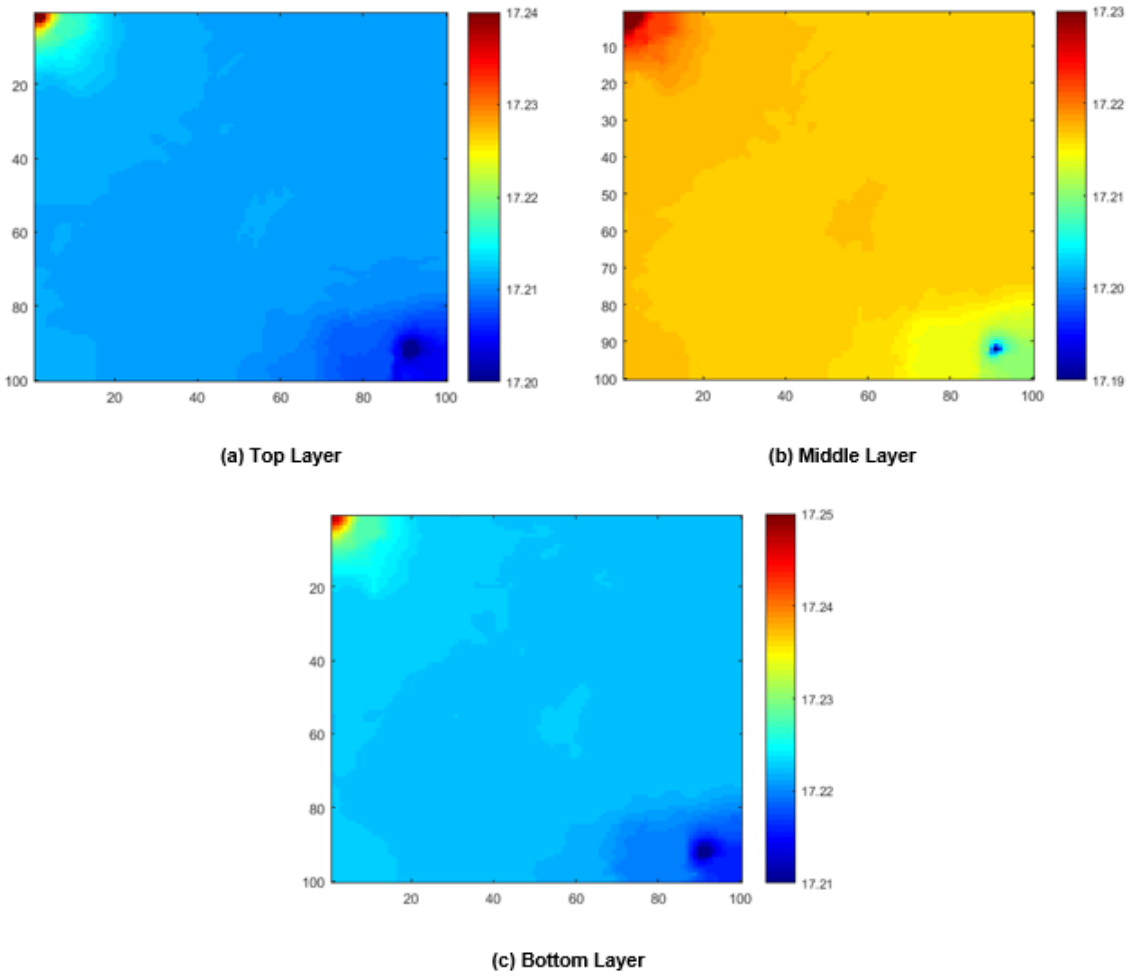

Figure 5.14: Logarithmic pressure distribution in the $100 \times 100 \times 3$ Naturally Fractured Carbonate Karst Reservoir at 100 days (Note that each graph is set to a different color scale to get the best contrast) [10].

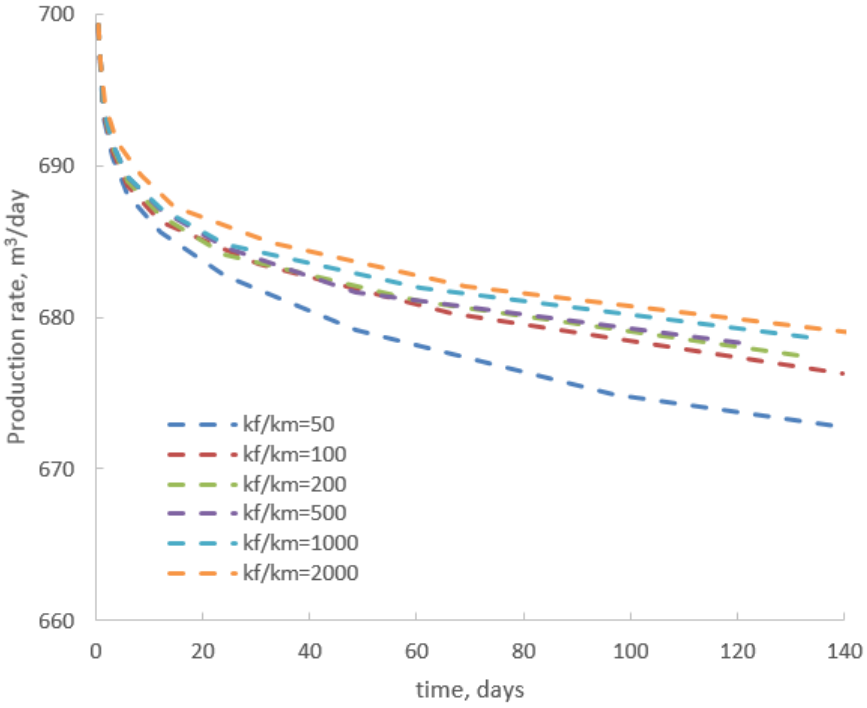

Figure 5.15: Volumetric production rate over time for different permeability ratios at stock-tank conditions [10].

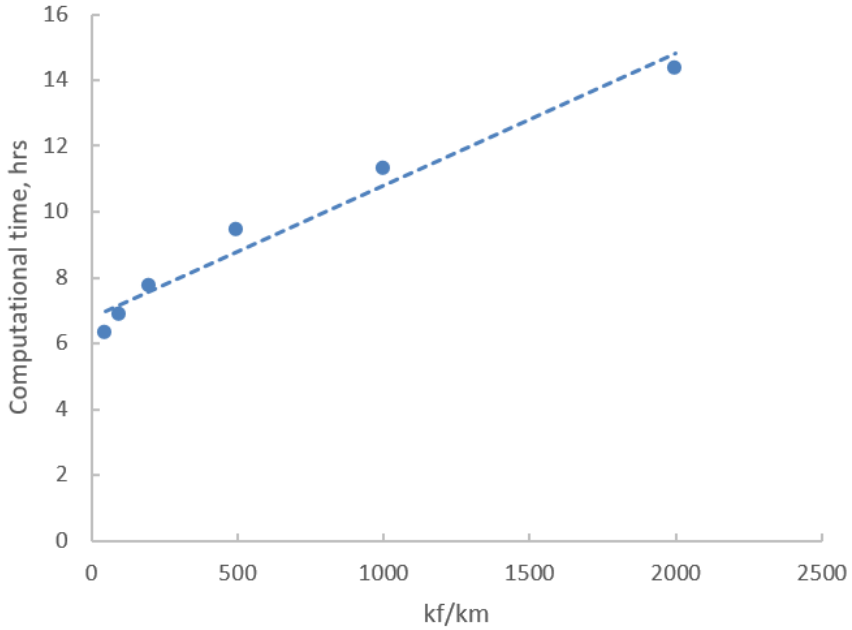

Figure 5.16: Computational time cost of the 3D reservoir model for different permeability ratios [10].

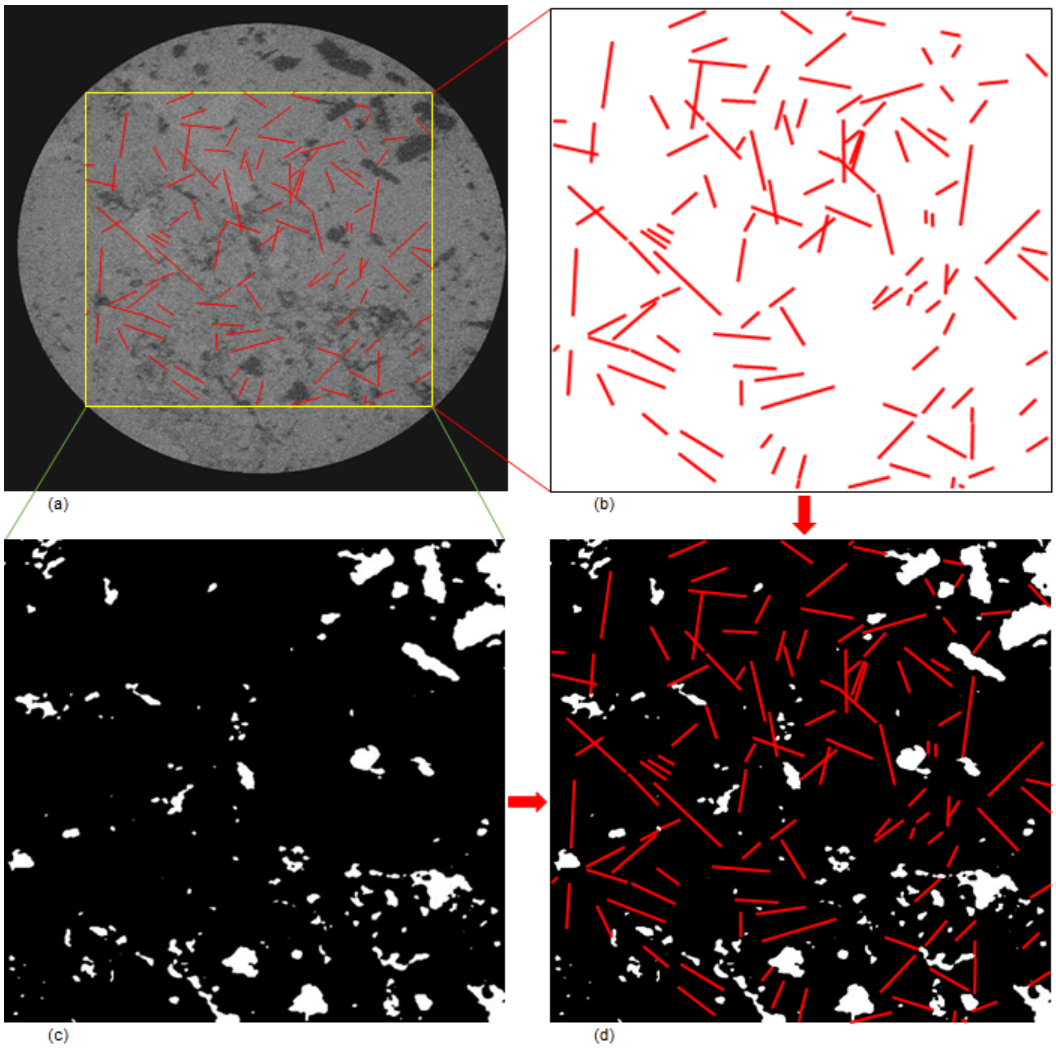

Figure 5.17: The micro-CT scan image with the fractures shown in red, (a). The fracture network in the cropped image; the yellow square in (a), (b). The cropped and segmented image; the yellow square in (a) with no fracture, (c). The final geological model having three structures, namely, fractures (red), Vugs (white), and matrix (black), (d) [11].

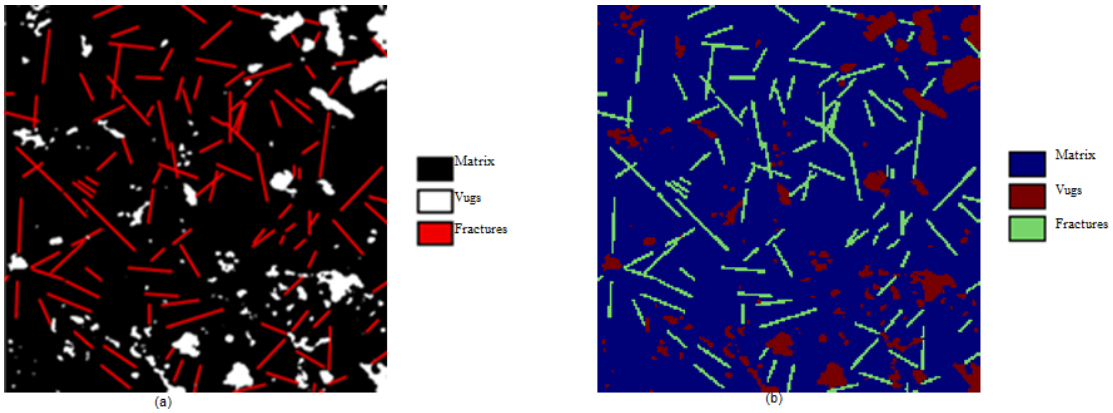

Figure 5.18: The reference geological model having a size of $192 \times 192 \times 1$ pixel, (a). The training image (i.e. the reference geological model in (a)) as it appears in SGeMS after converting it into GSLIB format using a developed training image converting code, (b) [11].

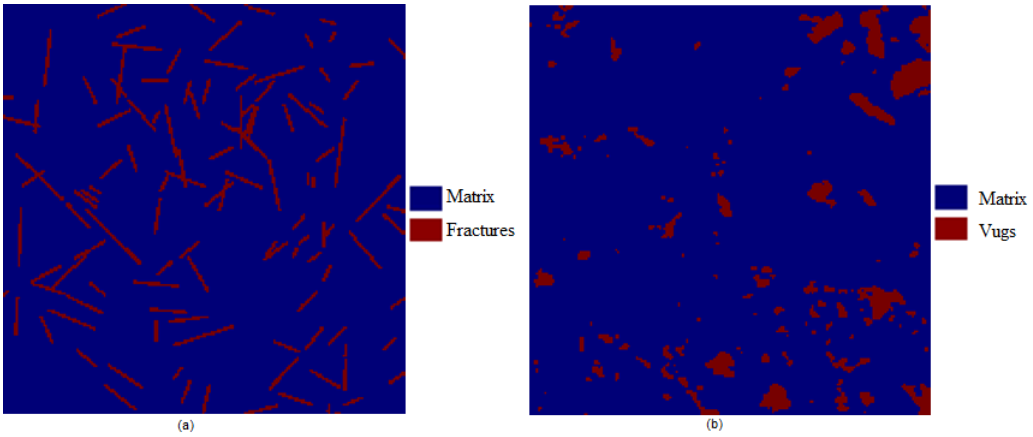

Figure 5.19: The new training images generated by separating the structures in the reference model into matrix-fracture, (a) and matrix-vugs, (b) [11].

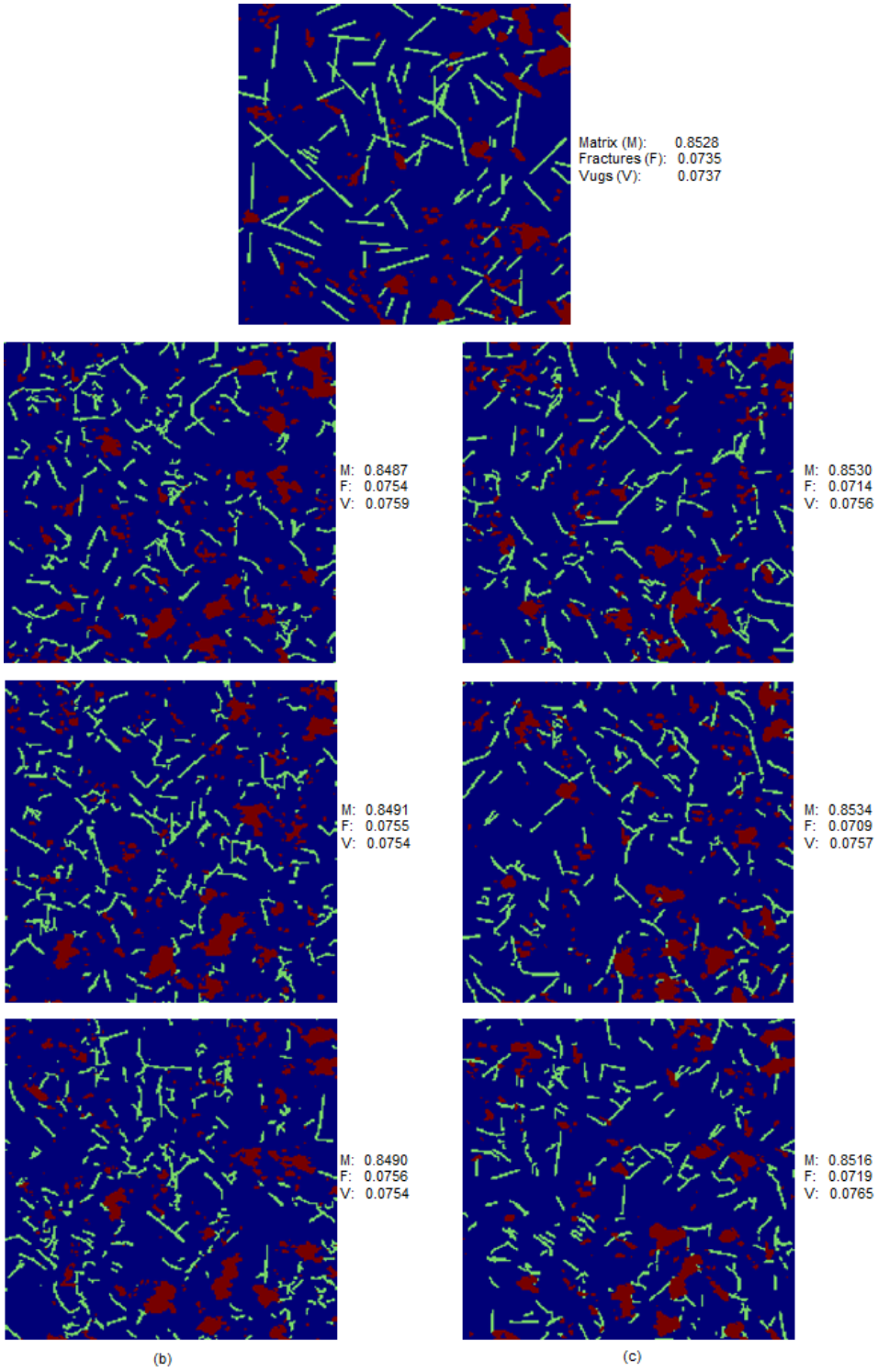

Figure 5.20: The reference model, (a), and example of MPG realizations generated from the direct, (column b), and the combination method, (column c) with the proportions of the three stractures in each model [11].

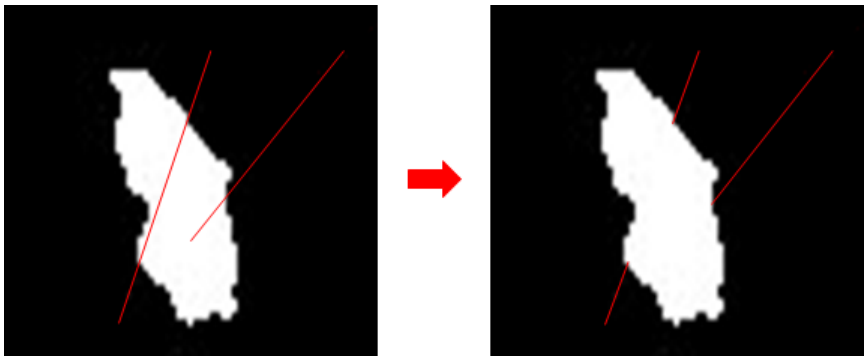

Figure 5.21: Illustration of how fracture-vug intersection is treated using a written VB code in the generation of the geological models by combining fracture networks with matrix-vug models [11].

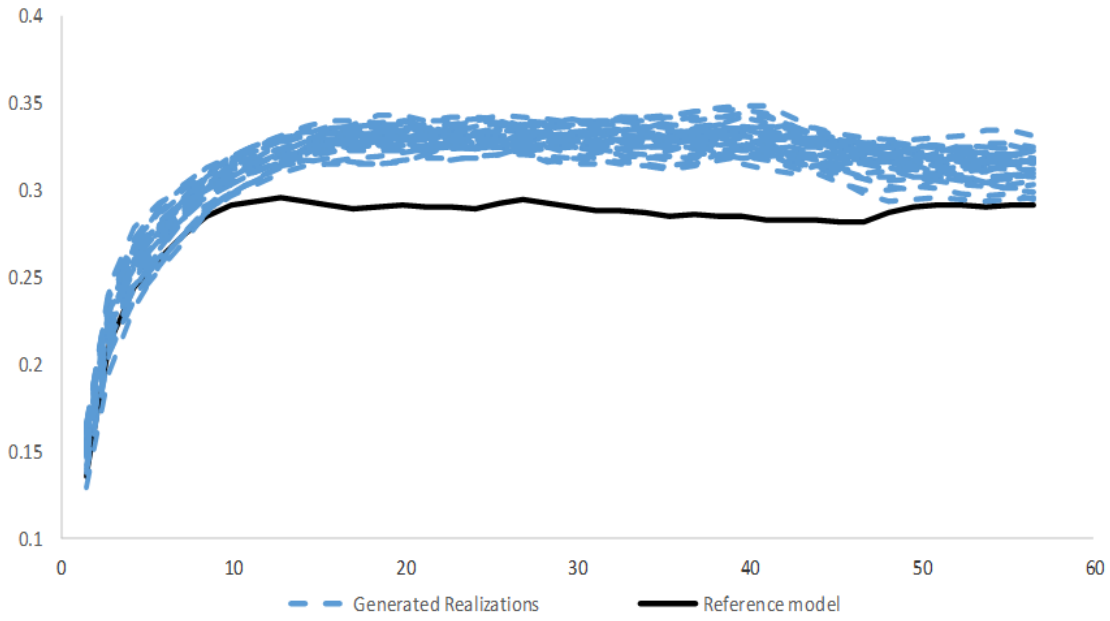

Figure 5.22: Variograms of the reference model and the realizations generated by the direct method [11].

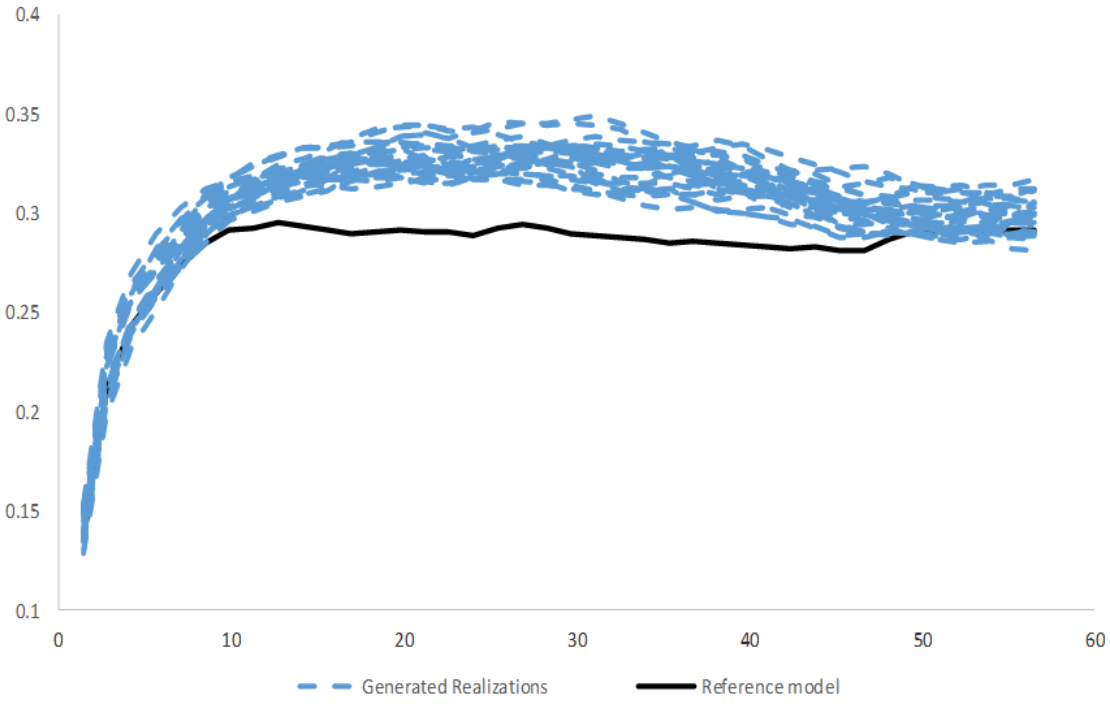

Figure 5.23: Variograms of the reference model and the realizations generated by the combination method [11].

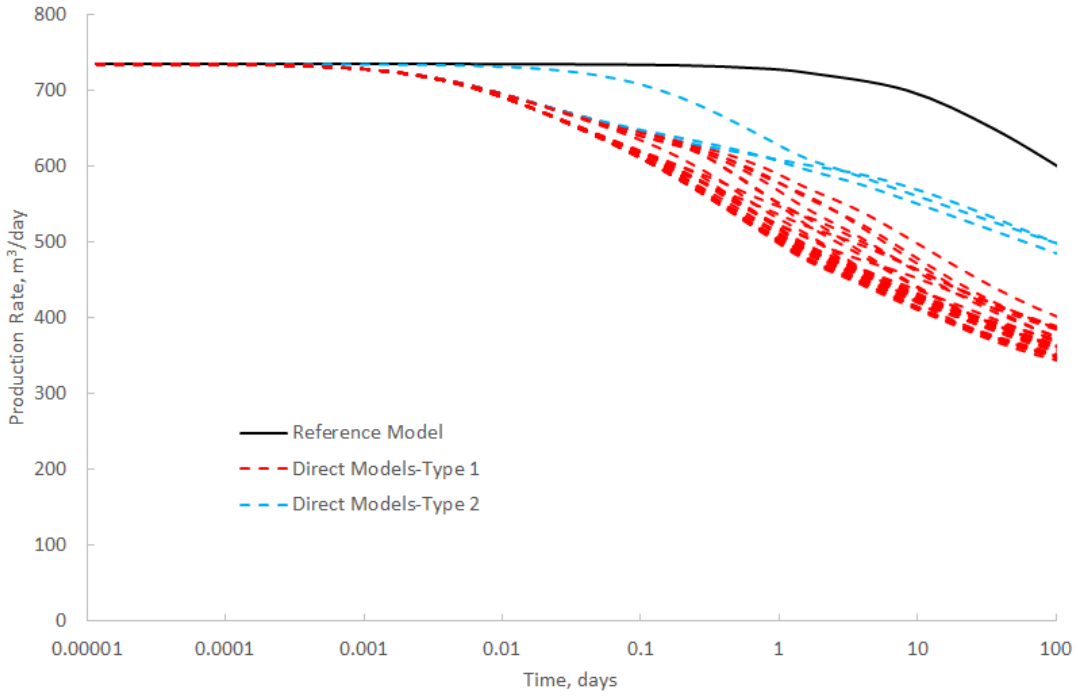

Figure 5.24: Flow performances of MPG realizations for direct models [11].

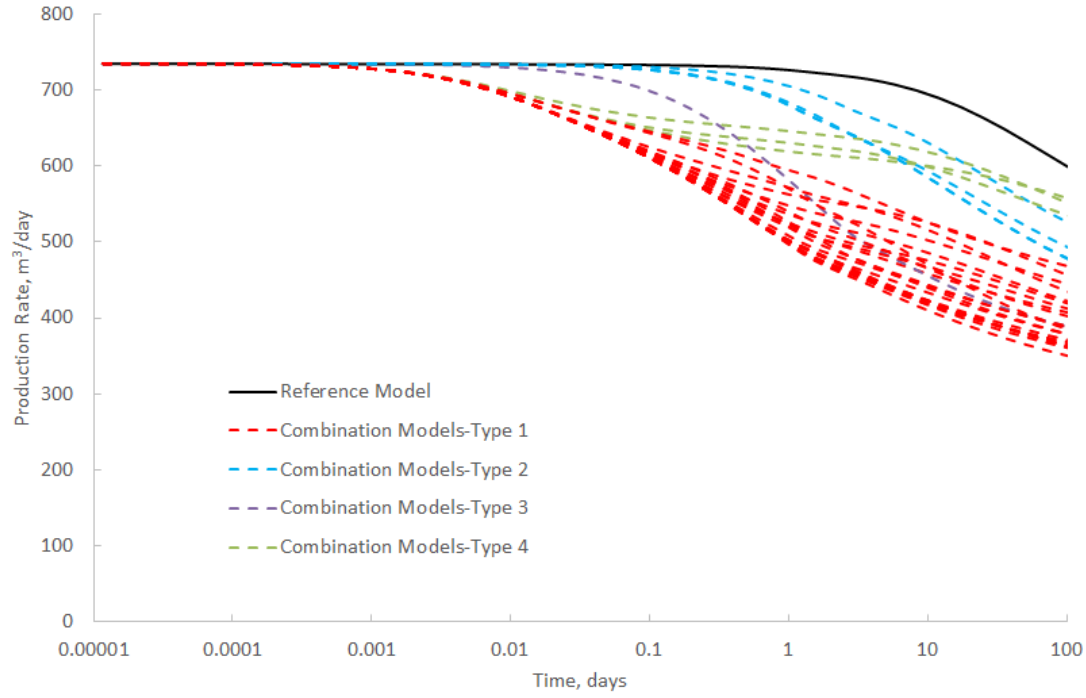

Figure 5.25: Flow performances of MPG realizations for combination models [11].

6. CONCLUSIONS

The Stokes-Brinkman equation has been pursued in recent years as a physical yet unified approach toward the simulation of coupled flow in naturally fractured carbonate karst reservoirs, but its application has been somehow restricted to steady-state flow. For the first time, we have proposed a transient Stokes-Brinkman model and lain the theoretical foundation for it, by discovering the applicability of the Stokes-Brinkman equation to transient flow through a detailed examination of its derivation process, and by incorporating a transient material balance equation which proves to be exact in the entire fractured karst reservoir. The finite difference formulation of the transient Stokes-Brinkman model has been derived, again for the first time, and an inhouse reservoir simulator is developed to actually solve this numerical problem.

Three fine-scale 2D reservoir models are used to illustrate the transient flow model. The first model demonstrates that the Stokes-Brinkman model can reduce to Darcy flow correctly, while the results of second and third models show that the Stokes-Brinkman model indeed yields different pressure distributions from Darcy's law, though the pressure differences are significant only around the wells. The 3D simulation results coincide with the 2D cases and imply that Darcy's law can be seen as a mathematical simplification of the Stokes-Brinkman equation, and according to the latter, we should not try to distinguish between connected and isolated vugs, nor should we estimate the fracture and karst permeability. Instead, it is sufficient to set fracture and karst permeability to $1000\ 2000$ times of the porous medium permeability, which produces satisfactory numerical results with reasonable computational cost. These results form the basis for future study of multi-phase and multi-scale flow cases.

6.1 Challenges

Many problems still need to be addressed for the numerical solution of the transient Stokes-Brinkman model, among which the most pressing is its computational inefficiency. The nonlinearity of the Stokes-Binkman equation requires the velocities to be solved for explicitly, so that our simulator has to use approximately four times as many unknown variables as traditional Darcy-type simulations do, resulting in more memory consumption and much longer computational time. To solve this problem, we aim at reformulating the finite difference schemes and optimizing the numerical algorithms. Expansion of the capacity of our simulator is also in the plan, which will enable us to investigate more sophisticated reservoir models.

6.2 Future Study

We have made a big step to bring the Stokes-Brinkman equation from steady-state to transient flow, and to show its close connection with the simpler Darcy's law. However, we have restricted ourselves to single-phase liquid flow so far, and need to further verify our conclusions in the context of compressible gas flow and even multiphase flow, and on top of that, we will be able to decide if upscaling and multisale generalizations of the Stokes-Brinkman model will be of interest. Moreover, it is also necessary to carefully benchmark our simulator against a commercial reservoir simulator, to ensure we get correct simulation results before proceeding to the next steps.

REFERENCES

[1] Schlumberger, "Carbonate reservoirs," Report, 2007. [Online]. Available: www.slb.com/carbonates

[2] BP, "BP statistical review of world energy," Report, 2016. [Online]. Available: bp.com/statisticalreview

[3] R. J. Dunham, *Classification of carbonate rocks according to depositional texture*, ser. AAPG Memoir. American Association of Petroleum Geologists, 1962, vol. 1, pp. 108–121.

[4] SEPM-STRATA, "The carbonate factory," 2013. [Online]. Available: http://www.sepmstrata.org/page.aspx?pageid=324

[5] P. W. Choquette and L. C. Pray, "Geologic nomenclature and classification of porosity in sedimentary carbonates," *AAPG Bulletin*, vol. 54, no. 2, pp. 207–244, 1970.

[6] W. Ahr, D. Allen, A. Boyd, H. Bachman, T. Smithson, E. Clerke, K. Gzara, J. Hassall, C. Murty, H. Zubari, and R. Ramamoorthy, "Confronting the carbonate conundrum," *Schlumberger Oilfield Review*, pp. 18–29, 2005.

[7] J. Bear, *Dynamics of Fluids in Porous Media*, revised ed., ser. Dover Civil and Mechanical Engineering. New York: Dover Publications, 1988. [Online]. Available: http://app.knovel.com/hotlink/toc/id:kpDFPM000I/dynamics-fluids-in-porous/dynamics-fluids-in-porous

[8] H. C. Brinkman, "A calculation of the viscous force exerted by a flowing fluid on a dense swarm of particles," *Applied Scientific Research*, vol. 1, no. 1, pp. 27–34, 1949.

[9] P. C. Carman, "Fluid flow through granular beds," *Chemical Engineering Research and Design*, vol. 75, pp. S32–S48, 1997.

[10] J. He, J. E. Killough, M. M. Fadlelmula F., and M. Fraim, "Unified finite difference modeling of transient flow in naturally fractured carbonate karst reservoirs - a 3D case study," in *SPE Proceedings*, ser. ATCE 2015. Houston, TX, USA: Society of Petroleum Engineers, 2015, Conference Paper.

[11] M. M. Fadlelmula F., M. Fraim, J. He, and J. E. Killough, "Discrete fracture-vug network modeling in naturally fractured vuggy reservoirs using multiple-point geostatistics: A micro-scale case," in *SPE Proceedings*, ser. ATCE 2015. Houston, TX, USA: Society of Petroleum Engineers, 2015, Conference Paper.

[12] C. L. Yaws, *Chemical Properties Handbook: Physical, Thermodynamics, Engironmental Transport, Safety & Health Related Properties for Organic & Inorganic Chemical*, 1st ed., ser. McGraw-Hill Handbooks. McGraw-Hill Professional, 1998.

[13] J. He, J. E. Killough, M. M. Fadlelmula F., and M. Fraim, "A unified finite difference model for the simulation of transient flow in naturally fractured carbonate karst reservoirs," in *SPE Proceedings*, ser. RSS 2015. Houston, TX, USA: Society of Petroleum Engineers, 2015, Conference Paper.

[14] W. Schlager, *Carbonate Sedimentology and Sequence Stratigraphy*. SEPM Society for Sedimentary Geology, 2005.

[15] Z. Sun, D. N. Espinoza, and M. T. Balhoff, "Discrete element modeling of indentation tests to investigate mechanisms of CO2-related chemomechanical rock alteration," *Journal of Geophysical Research: Solid Earth*, vol. 121, no. 11, pp. 7867–7881, 2016.

[16] J. He, Y. Chen, L. Zhengchun, and R. Samuel, "Global correlation of rock brittleness indices with petrophysical and geomechanical properties and its application to the prediction of rate of penetration (ROP)," in *SPE Proceedings*, ser. APDT 2016. Singapore: Society of Petroleum Engineers, 2016, Conference Paper.

[17] C. Dabbouk, A. Liaqat, G. Williams, and G. Beattie, "Waterflood in vuggy layer of a middle east reservoir - displacement physics understood," in *SPE Proceedings*, ser. ADIPEC 2002. Abu Dhabi, UAE: Society of Petroleum Engineers, 2002, Conference Paper.

[18] K. Tuncay, A. Park, G. Ozkan, X. Zhan, T. Hoak, K. Sundberg, and P. Ortoleva, "Models for naturally fractured, carbonate reservoir simulations," Report, December 1998. [Online]. Available: http://www.netl.doe.gov/kmd/cds/disk41/B%20-%20Reservoir%20Characterization/91008%2023%20Pt%203.pdf

[19] L. Zhang, S. L. Bryant, J. Jennings, James W., T. J. Arbogast, and R. Paruchuri, "Multiscale flow and transport in highly heterogeneous carbonates," in *SPE Proceedings*, ser. ATCE 2004. Houston, TX, USA: Society of Petroleum Engineers, 2004, Conference Paper.

[20] D. Abdassah and I. Ershaghi, "Triple-porosity systems for representing naturally fractured reservoirs," *SPE Formation Evaluation*, vol. 1, 1986.

[21] M. Bai, D. Elsworth, and J.-C. Roegiers, "Multiporosity/multipermeability approach to the simulation of naturally fractured reservoirs," *Water Resources Research*, vol. 29, no. 6, pp. 1621–1633, 1993.

[22] R. Camacho Velazquez, M. A. Vasquez-Cruz, R. Castrejon-Aivar, and V. Arana-Ortiz, "Pressure transient and decline curve behaviors in naturally fractured vuggy carbonate reservoirs," *SPE Reservoir Evaluation & Engineering*, vol. 8, no. 2, pp. 95 – 112, 2005.

[23] Z. Kang, Y.-S. Wu, J. Li, Y. Wu, J. Zhang, and G. Wang, "Modeling multiphase flow in naturally fractured vuggy petroleum reservoirs," in *SPE Proceedings*, ser. ATCE 2006. San Antonio, TX, USA: Society of Petroleum Engineers, 2006, Conference Paper.

[24] Y.-S. Wu, C. A. Ehlig-Economides, G. Qin, Z. Kang, W. Zhang, B. T. Ajayi, and Q. Tao, "A triple-continuum pressure-transient model for a naturally fractured vuggy reservoir," in *SPE Proceedings*, ser. ATCE 2007. Anaheim, CA, USA: Society of Petroleum Engineers, 2007, Conference Paper.

[25] Y.-S. Wu, G. Qin, R. E. Ewing, Y. Efendiev, Z. Kang, and Y. Ren, "A multiple-continuum approach for modeling multiphase flow in naturally fractured vuggy petroleum reservoirs," in *SPE Proceedings*, ser. IOGCEC 2006. Beijing, China: Society of Petroleum Engineers, 2006, Conference Paper.

[26] H. Tang, J. E. Killough, Z. Heidari, and Z. Sun, "A new technique to characterize fracture density by use of neutron porosity logs enhanced by electrically transported contrast agents," *SPE Journal*, 2017.

[27] L. Li, S. Khorsandi, R. T. Johns, and K. Ahmadi, "Multiple-mixing-cell method for three-hydrocarbon-phase displacements," *SPE Journal*, vol. 20, pp. 1339–1349, 2015.

[28] S. Gao, J. E. Killough, J. He, M. M. Fadlelmula F., Y. Wang, and M. L. Fraim, "A new approach for the simulation of fractured vuggy carbonate reservoir with an application to upscaling," in *SPE Proceedings*, ser. RCSC 2017. Abu Dhabi, UAE: Society of Petroleum Engineers, 2017, Conference Paper.

[29] I. E. Khvatova, A. Renaud, E. Golitsina, G. Malutina, G. Sansiev, and I. Kuzilov, "Simulation of complex carbonate field: Double medium vs. single medium -

kharyaga field case," in *SPE Proceedings*, ser. ROGC 2012. Moscow, Russia: Society of Petroleum Engineers, 2012, Conference Paper.

[30] Z. Huang, J. Yao, Y. Li, C. Wang, and X. Lü, "Permeability analysis of fractured vuggy porous media based on homogenization theory," *Science China Technological Sciences*, vol. 53, no. 3, pp. 839–847, 2010.

[31] J. Wang, H. Song, W. Zhu, J. He, and J. Killough, "A fractal-based model for relative permeability in nanoscale pores with interfacial effects," *Special Topics & Reviews in Porous Media*, vol. 7, no. 4, pp. 335–343, 2016.

[32] M. Alfi, B. Yan, Y. Cao, C. An, Y. Wang, J. He, and J. E. Killough, "How to improve our understanding of gas and oil production mechanisms in liquid-rich shale," in *SPE Proceedings*, ser. ATCE 2014. Amsterdam, the Netherlands: Society of Petroleum Engineers, 2014, Conference Paper.

[33] B. Yan, M. Alfi, Y. Wang, and J. E. Killough, "A new approach for the simulation of fluid flow in unconventional reservoirs through multiple permeability modeling," in *SPE Proceedings*, ser. ATCE 2013. New Orleans, LA, USA: Society of Petroleum Engineers, 2013, Conference Paper.

[34] B. Yan, Y. Wang, and J. E. Killough, "Beyond dual-porosity modeling for the simulation of complex flow mechanisms in shale reservoirs," *Computational Geosciences*, vol. 20, no. 1, pp. 69–91, 2016.

[35] J. Huang, C. Yang, X. Xue, and A. Datta-Gupta, "Simulation of coupled fracture propagation and well performance under different refracturing designs in shale reservoirs," in *SPE Proceedings*. Denver, CO, USA: Society of Petroleum Engineers, 2016, Conference Paper.

[36] J. Huang, A. Datta-Gupta, and J. R. Augustine, "Optimization of hydraulic fracture development and well performance using limited entry perforations," in *SPE Proceedings*, ser. SPE-POS OKC 2017. Oklahoma City, OK, USA: Society of Petroleum Engineers, 2017, Conference Paper.

[37] X. Jia, F. Zhang, and A. Filippov, "Effect of dynamic fracture conductivity during production," in *SPE Proceedings*, ser. WRM 2016. Anchorage, AK, USA: Society of Petroleum Engineers, 2016, Conference Paper.

[38] M. Oda, "An equivalent continuum model for coupled stress and fluid flow analysis in jointed rock masses," *Water Resources Research*, vol. 22, no. 13, pp. 1845–1856, 1986.

[39] T. G. Sitharam, J. Sridevi, and N. Shimizu, "Practical equivalent continuum characterization of jointed rock masses," *International Journal of Rock Mechanics and Mining Sciences*, vol. 38, no. 3, pp. 437–448, 2001.

[40] Y.-S. Wu, "On the effective continuum method for modeling multiphase flow, multicomponent transport, and heat transfer in fractured rock," in *Dynamics of Fluids in Fractured Rock*. American Geophysical Union, 2013, Book Section, pp. 299–312.

[41] J. Yao, Z. Huang, Y. Li, C. Wang, and X. Lü, "Discrete fracture-vug network model for modeling fluid flow in fractured vuggy porous media," in *SPE Proceedings*, ser. IOGCEC 2010. Beijing, China: Society of Petroleum Engineers, 2010, Conference Paper.

[42] T. Arbogast and D. Brunson, "A computational method for approximating a darcy-stokes system governing a vuggy porous medium," *Computational Geosciences*, vol. 11, no. 3, pp. 207–218, 2007.

[43] T. Arbogast and H. Lehr, "Homogenization of a darcy-stokes system modeling vuggy porous media," *Computational Geosciences*, vol. 10, no. 3, pp. 291–302, 2006.

[44] X. Peng, Z. Du, B. Liang, and Z. Qi, "Darcy-Stokes streamline simulation for the tahe-fractured reservoir with cavities," *SPE Journal*, vol. 14, no. 3, pp. 543–552, 2009.

[45] G. S. Beavers and D. D. Joseph, "Boundary conditions at a naturally permeable wall," *Journal of Fluid Mechanics*, vol. 30, no. 1, pp. 197–207, 1967.

[46] W. Jäger and A. Mikelić, "On the interface boundary condition of beavers, joseph, and saffman," *SIAM Journal on Applied Mathematics*, vol. 60, no. 4, pp. 1111–1127, 2000.

[47] P. G. Saffman, "On the boundary condition at the surface of a porous medium," *Studies in Applied Mathematics*, vol. 1, pp. 93–101, 1971.

[48] P. Popov, Y. Efendiev, and G. Qin, "Multiscale modeling and simulations of flows in naturally fractured karst reservoirs," *Communications in Computational Physics*, vol. 6, no. 1, pp. 162–184, 2009.

[49] P. Popov, L. Bi, Y. Efendiev, R. E. Ewing, G. Qin, J. Li, and Y. Ren, "Multi-physics and multi-scale methods for modeling fluid flow through naturally-fractured vuggy carbonate reservoirs," in *SPE Proceedings*, ser. MEOS 2007. Manama, Bahrain: Society of Petroleum Engineers, 2007, Conference Paper.

[50] A. F. Gulbransen, V. L. Hauge, and K.-A. Lie, "A multiscale mixed finite element method for vuggy and naturally fractured reservoirs," in *SPE Proceedings*, ser. RSS 2009. The Woodlands, TX, USA: Society of Petroleum Engineers, 2009, Conference Paper.

[51] A. F. Gulbransen, V. L. Hauge, and K. A. Lie, "A multiscale mixed finite element method for vuggy and naturally fractured reservoirs," *SPE Journal*, vol. 15, pp. 395–403, 2010.

[52] F. Golfier, C. Zarcone, B. Bazin, R. Lenormand, D. Lasseux, and M. Quintard, "On the ability of a Darcy-scale model to capture wormhole formation during the dissolution of a porous medium," *Journal of Fluid Mechanics*, vol. 457, no. 200242, pp. 213–254, 2002.

[53] V. Laptev, "Numerical solution of coupled flow in plain and porous media," Doctoral Thesis, 2003. [Online]. Available: https://kluedo.ub.uni-kl.de/frontdoor/index/index/docId/1531

[54] L. Bi, G. Qin, P. Popov, Y. Efendiev, and M. Espedal, "An efficient upscaling process based on a unified fine-scale multi-physics model for flow simulation in naturally fracture carbonate karst reservoirs," in *SPE Proceedings*, ser. RCSC 2009. Abu Dhabi, UAE: Society of Petroleum Engineers, 2009, Conference Paper.

[55] P. Popov, G. Qin, L. Bi, Y. Efendiev, R. E. Ewing, Z. Kang, and J. Li, "Multiscale methods for modeling fluid flow through naturally fractured carbonate karst reservoirs," in *SPE Proceedings*, ser. ATCE 2007. Anaheim, CA, USA: Society of Petroleum Engineers, 2007, Conference Paper.

[56] P. Popov, G. Qin, L. Bi, Y. Efendiev, R. E. Ewing, and J. Li, "Multiphysics and multiscale methods for modeling fluid flow through naturally fractured carbonate karst reservoirs," *SPE Reservoir Evaluation & Engineering*, vol. 12, 2009.

[57] G. Qin, L. Bi, P. Popov, Y. Efendiev, and M. Espedal, "An efficient upscaling procedure based on Stokes-Brinkman model and discrete fracture network method for naturally fractured carbonate karst reservoirs," in *SPE Proceedings*, ser. IOGCEC 2010. Beijing, China: Society of Petroleum Engineers, 2010, Conference Paper.

[58] G. Qin, B. Gong, L. Bi, and X.-h. Wu, "Multi-scale and multi-physics methods for numerical modeling of fluid flow in fractured formations," in *SPE Proceedings*, ser. EUROPEC 2011. Vienna, Austria: Society of Petroleum Engineers, 2011, Conference Paper.

[59] I. S. Ligaarden, M. Krotkiewski, K.-A. Lie, M. Pal, and D. W. Schmid, "On the Stokes-Brinkman equations for modeling flow in carbonate reservoirs," in *Proceedings of 12th European Conference on the Mathematics of Oil Recovery*. Oxford, UK: European Association of Geoscientists and Engineers, 2010, Conference Paper.

[60] J. He, J. E. Killough, S. Gao, M. M. Fadlelmula F., and M. L. Fraim, "Confronting the simulation of fluid flow in naturally fractured carbonate karst reservoirs," in *SPE Proceedings*, ser. ADIPEC 2016. Abu Dhabi, UAE: Society of Petroleum Engineers, 2016, Conference Paper.

[61] M. K. Hubbert, "Darcy's law and the field equations of the flow of underground fluids," in *Petroleum Transactions*. Dijon, France: American Institute of Mining, Metallurgical, and Petroleum Engineers, 1956, Conference Paper.

[62] L. Li, S. Khorsandi, R. T. Johns, and R. M. Dilmore, "CO2 enhanced oil recovery and storage using a gravity-enhanced process," *International Journal of Greenhouse Gas Control*, vol. 42, pp. 502–515, 2015.

[63] H. Darcy, *Les fo ntain es Publiques de lu Ville de Dijon*. Paris: Dalmont, 1856.

[64] L. Qi, H. ShamsiJazeyi, G. Ruan, J. A. Mann, Y.-H. Lin, C. Song, Y. Ma, L. Wang, J. M. Tour, G. J. Hirasaki, and R. Verduzco, "Segregation of amphiphilic polymer-coated nanoparticles to bicontinuous oil/water microemulsion phases," *Energy & Fuels*, vol. 31, pp. 1339–1346, 2017.

[65] R. B. Bird, W. E. Stewart, and E. N. Lightfoot, *Transport Phenomena*, 2nd ed. John Wiley & Sons, Inc, 2006.

[66] C. J. Glover and H. Jones, *Conservation Principles for Continuous Media*, 3rd ed. McGraw-Hill, 1994.

[67] G. Buresti, "A note on Stokes' hypothesis," *Acta Mechanica*, vol. 226, no. 10, pp. 3555–3559, 2015.

[68] M. Gad-el Hak, "Questions in fluid mechanics: Stokes' hypothesis for a Newtonian, isotropic fluid," *Journal of Fluids Engineering*, vol. 117, no. 1, pp. 3–5, 1995.

[69] E. Fathi, A. Tinni, and I. Y. Akkutlu, "Correction to Klinkenberg slip theory for gas flow in nano-capillaries," *International Journal of Coal Geology*, vol. 103, pp. 51–59, 2012.

[70] L. J. Klinkenberg, "The permeability of porous media to liquids and gases," in *Drilling and Production Practice*. New York, NY, USA: American Petroleum Institute, 1941, Conference Paper.

[71] A. Beskok and G. E. Karniadakis, "Report: A model for flows in channels, pipes, and ducts at micro and nano scales," *Microscale Thermophysical Engineering*, vol. 3, no. 1, pp. 43–77, 1999.

[72] D. R. Kincaid and E. W. Cheney, *Numerical Analysis: Mathematics of Scientific Computing*, 3rd ed. American Mathematical Society, 2002.

[73] P. D. Lax and R. D. Richtmyer, "Survey of the stability of linear finite difference equations," *Communications on Pure and Applied Mathematics*, vol. 9, pp. 267–293, 1956.

[74] J. Nocedal and S. Wright, *Numerical Optimization*, 2nd ed., ser. Springer Series in Operations Research and Financial Engineering. Springer, 2006.

[75] E. E. Rosinger, "What is wrong with the Lax-Richtmyer fundamental theorem of linear numerical analysis?" *eprint arXiv:math/0507288*, 2005.

[76] T. Arbogast, M. F. Wheeler, and I. Yotov, "Mixed finite elements for elliptic problems with tensor coefficients as cell-centered finite differences," *SIAM Journal on Numerical Analysis*, vol. 34, no. 2, pp. 828–852, 1997.

[77] M. Vohralik, "Equivalence between lowest-order mixed finite element and multipoint finite volume methods on simplicial meshes," *ESAIM: Mathematical Modelling and Numerical Analysis*, vol. 40, no. 2, pp. 367 – 391, 2006.

[78] G. J. Moridis and C. M. Freeman, "The RealGas and RealGasH2O options of the TOUGH+ code for the simulation of coupled fluid and heat flow in tight/shale gas systems," *Computers & Geosciences*, vol. 65, pp. 56–71, 2014.

[79] L. Ju and J. Burkardt, "Restarted GMRES solver for sparse linear systems," 2012. [Online]. Available: http://people.sc.fsu.edu/~jburkardt/cpp_src/mgmres/mgmres.html

[80] Y. Sadd, *Iterative Methods for Sparse Linear Systems*, 2nd ed. Society for Industrial and Applied Mathematics, 2003.

[81] M. R. Hestenes and E. Stiefel, "Methods of conjugate gradients for solving linear systems," *Journal of Research of the National Bureau of Standards*, vol. 49, no. 6, pp. 409–436, 1952.

[82] A. Datta-Gupta and M. J. King, *Streamline Simulation : Theory and Practice*, ser. SPE Textbook Series Vol. 11. Richardson, TX: Society of Petroleum Engineers, 2007.

[83] M. M. Fadlelmula F., J. E. Killough, and M. Fraim, "TiConverter: A training image converting tool for multiple-point geostatistics," *Computers & Geosciences*, vol. 96,

pp. 47–55, 2016.

[84] N. Remy, A. Boucher, and J. Wu, *Applied Geostatistics with SGeMS: A User's Guide*. Cambridge University Press, 2009.

[85] S. A. Castro, "A probabilistic approach to jointly integrate 3D/4D seismic, production data and geological information for building reservoir models," Doctoral Thesis, 2007. [Online]. Available: https://pangea.stanford.edu/ERE/pdf/pereports/PhD/Castro07.pdf

[86] M. M. Fadlelmula F., S. Qian, Y. Wang, M. Fraim, J. He, S. Gao, and J. E. Killough, "Separable multiple-point geostatistical modeling of three-dimensional discrete fracture-vug networks," in *SPE Proceedings*, ser. ADIPEC 2016. Abu Dhabi, UAE: Society of Petroleum Engineers, 2016, Conference Paper.

[87] J. Shu, "Comparison of various techniques for computing well index," Report, 2005. [Online]. Available: searchworks.stanford.edu/view/6425735

[88] F. Zhang, S. Miska, M. Yu, E. Ozbayoglu, and N. Takach, "Pressure profile in annulus: Solids play a significant role," *Journal of Energy Resources Technology*, vol. 137, no. JERT-14-1293, 2015.

[89] X. Jia and F. Zhang, "Applying data-driven method to production decline analysis and forecasting," in *SPE Proceedings*, ser. ATCE 2016. Dubai, UAE: Society of Petroleum Engineers, 2016, Conference Paper.